Royal Netherlands
Meteorological Institute
Ministry of Infrastructure
and Water Management

Ozone Monitoring Instrument Algorithm Theoretical Basis Document of the Aerosol Direct Radiative Effect over clouds

document number	:	OMI-KNMI-L2-0000-DRE
authors	:	M. de Graaf
CI identification	:	*None*
issue	:	1.0.0
date	:	2022-08-01
status	:	Released

Document approval record

	digital signature
Prepared:	
Checked:	Martin de Graaf Digitally signed by Martin de Graaf Date: 2022.08.01 11:06:19 +02'00'
Approved PM:	
Approved PI:	

Document change record

issue	date	item	comments
0.0.1	2020-04-14	All	Initial version
1.0.0	2022-08-01	All	Release

Contents

List of Tables

List of Figures

1 Introduction

1.1 Identification

This document is identified as OMI-KNMI-L2-0000-DRE.

1.2 Purpose and objective

The purpose of this document is to describe the theoretical basis and the implementation of the OMI Level-2 Aerosol Direct Radiative Effect algorithm for OMI, combined with collocated MODIS measurements.

1.3 Document overview

[*generic description of the document*]

2 Applicable and reference documents

2.1 Reference documents

[RD1] M. de Graaf, L. G. Tilstra, I. Aben *et al.*; Satellite observations of the seasonal cycles of absorbing aerosols in Africa related to the monsoon rainfall, 1995 - 2008. *Atmos. Environ.*; **44** (2010) (10), 1274; 10.1016/j.atmosenv.2009.12.038.

[RD2] G. R. van der Werf, J. T. Randerson, L. Giglio *et al.*; Global fire emissions and the contribution of deforestation, savanna, forest, agricultural, and peat fires (1997–2009). *Atmos. Chem. Phys.*; **10** (2010) (23), 11707; 10.5194/acp-10-11707-2010.

[RD3] R. Swap, M. Garstang, S. A. Macko *et al.*; The long-range transport of southern African aerosols to the tropical South Atlantic. *J. Geophys. Res.*; **101** (1996), D19; 10.1029/95JD01049.

[RD4] M. de Graaf, L. G. Tilstra, P. Wang *et al.*; Retrieval of the aerosol direct radiative effect over clouds from spaceborne spectrometry. *J. Geophys. Res.*; **117** (2012) (D7); 10.1029/2011JD017160.

[RD5] Glenn Rolph, Ariel Stein and Barbara Stunder; Real-time Environmental Applications and Display sYstem: READY. *Environ. Modell. Softw.*; **95** (2017), 210 ; 10.1016/j.envsoft.2017.06.025.

[RD6] Chamara Rajapakshe, Zhibo Zhang, John E. Yorks *et al.*; Seasonally transported aerosol layers over southeast Atlantic are closer to underlying clouds than previously reported. *Geophysical Research Letters*; **44** (2017) (11), 5818; 10.1002/2017GL073559.

[RD7] M. de Graaf, L.G. Tilstra and P. Stammes; Aerosol direct radiative effect over clouds from synergic OMI and MODIS reflectances. *Atmos. Meas. Tech.*; **2019** (2019), 5119 ; 10.5194/amt-12-5119-2019. URL `https://doi.org/10.5194/amt-12-5119-2019`.

[RD8] K. N. Liou; *An Introduction to Atmospheric Radiation* (Academic Press, 2002).

[RD9] M. de Graaf, Holger Sihler, L. G. Tilstra *et al.*; How big is an OMI pixel? *Atmos. Meas. Tech.*; (2016); 10.5194/amt-9-3607-2016. URL `http://www.atmos-meas-tech.net/9/3607/2016/`.

[RD10] H. Sihler, P. Lübcke, R. Lang *et al.*; In-operation field-of-view retrieval (IFR) for satellite and ground-based DOAS-type instruments applying coincident high-resolution imager data. *Atmos. Meas. Tech.*; **10** (2017) (3), 881; 10.5194/amt-10-881-2017. URL `https://www.atmos-meas-tech.net/10/881/2017/`.

[RD11] Teruyuki Nakajima and Michael D. King; Determination of the Optical Thickness and Effective Particle Radius of Clouds from Reflected Solar Radiation Measurements: Part I: Theory. *J. Atmos. Sci.*; **47** (1990) (15), 1878; 10.1175/1520-0469(1990)047<1878:DOTOTA>2.0.CO;2.

[RD12] Jim M. Haywood, Simon R. Osborne and Steven J. Abel; The effect of overlying absorbing aerosol layers on remote sensing retrievals of cloud effective radius and cloud optical depth. *Q. J. R. Meteorol. Soc.*; **130** (2004), 779; 10.1256/qj.03.100.

[RD13] Kerry Meyer, Steven Platnick and Zhibo Zhang; Simultaneously inferring above-cloud absorbing aerosol optical thickness and underlying liquid phase cloud optical and microphysical properties using MODIS. *J. Geophys. Res.*; **120** (2015) (11), 5524; 10.1002/2015JD023128.

[RD14] M. de Graaf, P. Stammes, O. Torres *et al.*; Absorbing Aerosol Index: Sensitivity Analysis, application to GOME and comparison with TOMS. *J. Geophys. Res.*; **110** (2005), D01201; 10.1029/2004JD005178.

[RD15] Jim M. Haywood, Simon R. Osborne, P. N. Francis *et al.*; The mean physical and optical properties of regional haze dominated by biomass burning aerosol measured from the C–130 aircraft during SAFARI 2000. *J. Geophys. Res.*; **108** (2003), D13; 10.1029/2002JD002226.

[RD16] Thomas W. Kirchstetter, T. Novakov and Peter V. Hobbs; Evidence that the spectral dependence of light absorption by aerosols is affected by organic carbon. *J. Geophys. Res.*; **109** (2004), D21208; 10.1029/2004JD004999.

[RD17] R. W. Bergstrom, P. Pilewskie, P. B. Russell *et al.*; Spectral absorption properties of atmospheric aerosols. *Atmos. Chem. Phys.*; **7** (2007) (23), 5937; 10.5194/acp-7-5937-2007.

[RD18] P. B. Russell, R. W. Bergstrom, Y. Shinozuka *et al.*; Absorption Angstrom Exponent in AERONET and related data as an indicator of aerosol composition. *Atmos. Chem. Phys.*; **10** (2010) (3), 1155; 10.5194/acp-10-1155-2010.

[RD19] H. Jethva and O. Torres; Satellite-based evidence of wavelength-dependent aerosol absorption in biomass burning smoke inferred from Ozone Monitoring Instrument. *Atmos. Chem. Phys.*; **11** (2011), 10541; 10.5194/acp-11-10541-2011.

[RD20] Impact of above-cloud aerosols on the angular distribution pattern of cloud bidirectional-reflectance and implication for above-cloud aerosol direct radiative effect.
source: University of Maryland; **ref:** Prouty, Jr., Roy Edward.

[RD21] N. Benas, J. F. Meirink, M. Stengel *et al.*; Sensitivity of liquid cloud optical thickness and effective radius retrievals to cloud bow and glory conditions using two SEVIRI imagers. *Atmos. Meas. Tech. Disc.*; **2019** (2019), 1; 10.5194/amt-2018-439.

[RD22] S. Platnick, M.D. King, S.A. Ackerman *et al.*; The MODIS cloud products: algorithms and examples from Terra. *IEEE Geosci. Remote Sens.*; **41** (2003) (2), 459; 10.1109/TGRS.2002.808301.

[RD23] Kazuaki Kawamoto, Teruyuki Nakajima and Takashi Y. Nakajima; A Global Determination of Cloud Microphysics with AVHRR Remote Sensing. *J. Climate*; **14** (2001) (9), 2054; 10.1175/1520-0442.

[RD24] R. A. Roebeling, A. J. Feijt and P. Stammes; Cloud property retrievals for climate monitoring: Implications of differences between Spinning Enhanced Visible and Infrared Imager (SEVIRI) on METEOSAT-8 and Advanced Very High Resolution Radiometer (AVHRR) on NOAA-17. *J. Geophys. Res.*; **111** (2006), D20210; 10.1029/2005JD006990.

[RD25] A. A. Kokhanovsky, V. V. Rozanov, J. P. Burrows *et al.*; The SCIAMACHY cloud products: Algorithms and examples from ENVISAT. *Adv. Space Res.*; **36** (2005), 789; 10.1016/j.asr.2005.03.026.

[RD26] D. Chand, R. Wood, T. L. Anderson *et al.*; Satellite-derived direct radiative effect of aerosols dependent on cloud cover. *Nat. Geosci.*; **2** (2009); 10.1038/NGEO437.

[RD27] M. de Graaf, N. Bellouin, L. G. Tilstra *et al.*; Aerosol direct radiative effect of smoke over clouds over the southeast Atlantic Ocean from 2006 to 2009. *Geophys. Res. Lett.*; **41** (2014) (21), 7723; 10.1002/2014GL061103.

[RD28] M. de Graaf, R. Schulte, F. Peers *et al.*; Comparison of Aerosol Direct Effect over clouds. *Atmos. Chem. Phys. Disc.*; **2019** (2020), 1; 10.5194/acp-2019-545. URL `https://www.atmos-chem-phys-discuss.net/acp-2019-545/`.

[RD29] F. Peers, F. Waquet, C. Cornet *et al.*; Absorption of aerosols above clouds from POLDER/PARASOL measurements and estimation of their direct radiative effects. *Atmos. Chem. Phys.*; **15** (2015), 4179; 10.5194/acp-15-4179-2015.

[RD30] Myhre, G., T. K. Berntsen *et al.*; Modeling the solar radiative impact of aerosols from biomass burning during the Southern African Regional Science Initiative (SAFARI-2000) experiment. *J. Geophys. Res.*; **108** (2003), D13; 10.1029/2002JD002313.

[RD31] Radiative transfer code development. Applications to the estimation of the radiative impact of aerosols.
source: Université Pierre et Marie Curie and Freien Universität Berlin; **ref:** Doppler.

[RD32] P. Y. Deschamps, F. M. Breon, M. Leroy *et al.*; The POLDER mission: instrument characteristics and scientific objectives. *IEEE Transactions on Geoscience and Remote Sensing*; **32** (1994) (3), 598; 10.1109/36.297978.

[RD33] F. Waquet, F. Peers, F. Ducos *et al.*; Global analysis of aerosol properties above clouds. *Geophys. Res. Lett.*; **40** (2013) (21), 5809; 10.1002/2013GL057482.

[RD34] D. Chand, T. L. Anderson, R. Wood *et al.*; Quantifying above-cloud aerosol using spaceborne lidar for improved understanding of cloud-sky direct climate forcing. *J. Geophys. Res.*; **113** (2008), D13206; 10.1029/2007JD009433.

[RD35] Hongbin Yu and Zhibo Zhang; New Directions: Emerging satellite observations of above-cloud aerosols and direct radiative forcing. *Atmos. Environ.*; **72** (2013), 36; http://dx.doi.org/10.1016/j.atmosenv.2013.02.017.

[RD36] K. Meyer, S. Platnick, L. Oreopoulos *et al.*; Estimating the direct radiative effect of absorbing aerosols overlying marine boundary layer clouds in the southeast Atlantic using MODIS and CALIOP. *J. Geophys. Res.*; **118** (2013), 4801; 10.1002/jgrd.50449.

[RD37] J. Lenoble, D. Tanré, P. Y. Deschamps *et al.*; A Simple Method to Compute the Change in Earth-Atmosphere Radiative Balance Due to a Stratospheric Aerosol Layer. *J. Atmos. Sci.*; **39** (1982) (11), 2565; 10.1175/1520-0469(1982)039<2565:ASMTCT>2.0.CO;2.

[RD38] Z. Ahmad, P. K. Bhartia and N. Krotkov; Spectral properties of backscattered UV radiation in cloudy atmospheres. *J. Geophys. Res.*; **109** (2004), D01201; 10.1029/2003JD003395.

[RD39] F. Peers, P. Francis, C. Fox *et al.*; Observation of absorbing aerosols above clouds over the south-east Atlantic Ocean from the geostationary satellite SEVIRI – Part 1: Method description and sensitivity. *Atmos. Chem. Phys.*; **19** (2019) (14), 9595; 10.5194/acp-19-9595-2019.

[RD40] Paquita Zuidema, Arthur J. Sedlacek III, Connor Flynn *et al.*; The Ascension Island Boundary Layer in the Remote Southeast Atlantic is Often Smoky. *Geophys. Res. Lett.*; **45** (2018) (9), 4456; 10.1002/2017GL076926. URL `https://agupubs.onlinelibrary.wiley.com/doi/abs/10.1002/2017GL076926`.

[RD41] Paquita Zuidema, Jens Redemann, James Haywood *et al.*; Smoke and Clouds above the Southeast Atlantic: Upcoming Field Campaigns Probe Absorbing Aerosol's Impact on Climate. *Bull. Am. Meteor. Soc.*; **97** (2016) (7), 1131; 10.1175/BAMS-D-15-00082.1.

[RD42] H. Jethva, O. Torres, L. A. Remer *et al.*; A Color Ratio Method for Simultaneous Retrieval of Aerosol and Cloud Optical Thickness of Above-Cloud Absorbing Aerosols From Passive Sensors: Application to MODIS Measurements. *IEEE T. Geosci. Remote*; **51** (2013) (7), 3862; 10.1109/TGRS.2012.2230008.

[RD43] D. M. Giles, A. Sinyuk, M. G. Sorokin *et al.*; Advancements in the Aerosol Robotic Network (AERONET) Version 3 database – automated near-real-time quality control algorithm with improved cloud screening for Sun photometer aerosol optical depth (AOD) measurements. *Atmos. Meas. Tech.*; **12** (2019) (1), 169; 10.5194/amt-12-169-2019.

3 References, terms and acronyms

3.1 Terms, definitions and abbreviated terms

AAI	Absorbing Aerosol Index
AAOT	Aerosol Absorption Optical Thickness
AOD	Aerosol Optical (Penetration) Depth
AOT	Aerosol Optical Thickness (partial - layer or total - atmosphere)
ATBD	Algorithm Theoretical Baseline Document
BRDF	Bidirectional Reflectance Distribution Function
BSA	Black-Sky Albedo
CAMS	Copernicus Atmosphere Monitoring Service
CF	Climate and Forecast metadata conventions
DAK	Doubling-Adding KNMI
DU	Dobson Units, 2.69×10^{16} molecules cm^{-2}
ECMWF	European Centre for Medium-Range Weather Forecast
ENVISAT	Environmental Satellite
EOS-Aura	Earth Observing System – Aura satellite
EPS-SG	EUMETSAT Polar System – Second Generation
ERS	European Remote Sensing Satellite
ESA	European Space Agency
EUMETSAT	European Organisation for the Exploitation of Meteorological Satellites
FOV	Field-of-View
FRESCO	Fast Retrieval Scheme for Clouds from the Oxygen A band
GMTED2010	Global Multi-resolution Terrain Elevation Data 2010
GOME	Global Ozone Monitoring Experiment
HDF	Hierarchical Data Format
KNMI	Koninklijk Nederlands Meteorologisch Instituut
LER	Lambertian-Equivalent Reflectivity
LUT	Look-Up Table
L2OP	Level-2 Operational Processor
L2PP	Level-2 Prototype Processor
MERIS	Medium Resolution Imaging Spectrometer
METOP	Meteorological Operational Satellite
MLS	Mid-Latitude Summer
NASA	National Aeronautics and Space Administration
NISE	Near-real-time Ice and Snow Extent
NRT	Near-Real-Time
OMI	Ozone Monitoring Instrument
PAM	Performance Assessment Module
RAA	Relative Azimuth Angle
RMSE	Root-Mean-Square Error
RTM	Radiative Transfer Model
SAA	Solar Azimuth Angle
SCIAMACHY	Scanning Imaging Absorption Spectrometer for Atmospheric Chartography
SW	Software
SZA	Solar Zenith Angle
S5	Sentinel-5 mission

S5P	Sentinel-5 Precursor mission
TOA	Top-of-Atmosphere
TOMS	Total Ozone Mapping Spectrometer
TROPOMI	Tropospheric Monitoring Instrument
UTC	Coordinated Universal Time
UV	Ultraviolet
UVNS	Ultraviolet Visible Near-infrared Shortwave spectrometer
VAA	Viewing Azimuth Angle
VIS	Visible
VZA	Viewing Zenith Angle

4 OMI Instrument description

A description of the OMI instrument and performance can be found in: .

5 MODIS Instrument description

A description of the MODIS instrument and performance can be found in: .

6 Introduction to the Aerosol DRE product

6.1 Background

The aerosol Direct Radiative Effect (DRE) quantifies the energy change due to aerosols interacting with (solar) radiation. The product described here quantifies the amount of energy that is absorbed by smoke that is present above cloud layers, directly interacting with the incoming solar radiation and the radiation reflected by the clouds.

The satellite product DRE is a combination of measurements by the satellite instruments OMI and MODIS, flying within approxamitely 8–15 minutes from each other (see section 4 for details), in an afternoon polar-orbiting constellation. Therefore, the aerosol DRE is measured only once per day for a location on the Earth, and always during the local afternoon (approximately 13.30 local time). Combining measurements from these

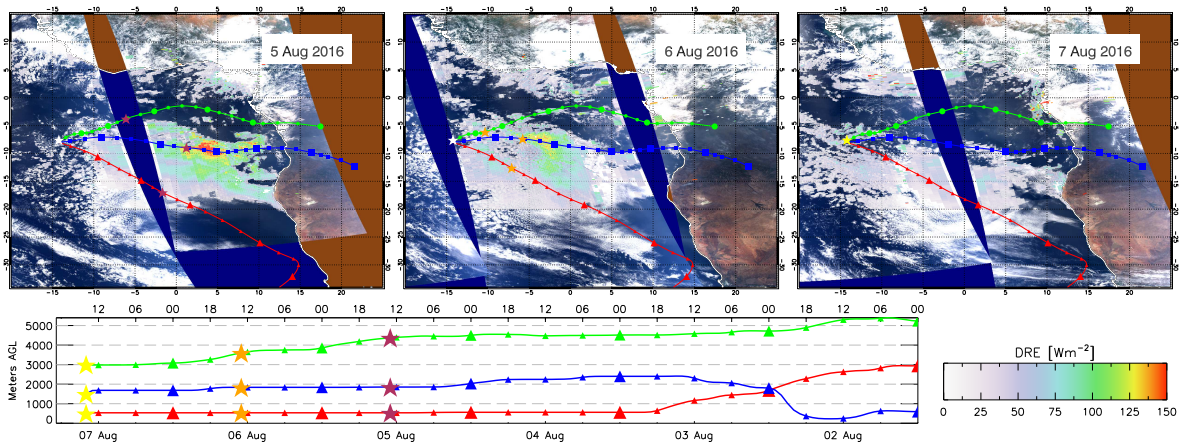

Figure 1: Aerosol DRE over clouds over the southeast Atlantic Ocean during 5–7 August 2016, combined with backtrajectories from the HYSPLIT model, indicating air parcels ending at 500 m (red), 1500 m (blue), and 3000 m (green) at Ascension Island. The position of the air in the backtrajectories during the satellite overpasses is indicated by the coloured stars (yellow on 7 August (at Ascension Island), orange on 6 August, and brown on 5 August).

two instruments is a computationally very demanding task, and the area for which the aerosol DRE was computed is small, only a large part of the southeast Atlantic Ocean is covered, for all other areas the product is not available. The measurements from the instruments cover the entire shortwave (solar) spectrum (ultraviolet - visible - shortwave infrared), at a high to moderate resolution, so only shorwave absorbed energy is considered. Longwave radiation (emitted by the Earth and atmosphere) is not considered. This means that only small aerosols (i.e. having similar size as the wavelengths of the radiation) are considered here. The most common small sized aerosol found in the area is smoke from biomass burning, and absorption will be assumed to have been due to smoke only. Desert dust, which is also commonly present over the Atlantic, is excluded from the consideration, but dust also absorbs solar energy and introduces uncertainties in the attribution of the product. Smoke absorbs most strongly in the UV, and the absorbed energy is typically highest in the UV. The smoke source over the Atlantic Ocean is typically biomass burning on the African continent during the monsoon dry season [RD1]. Therefore, the aerosol DRE is only computed for the months June–October. During the dry season a myriad of vegetation fires produces immense amounts of smoke, which is the single largest source of black carbon and natural carbonaceous species in the atmosphere worldwide (about 25 Tg black carbon annually [RD2]). The smoke can drift over the Atlantic during westerly circulations. It is most often found in a layer between about 1–5 km altitude, above the marine boundary layer [RD3, RD4].

The aerosol DRE over clouds is therefore defined as the instantaneous energy change due to radiation absorption by smoke above clouds. It is expressed in Wm^{-2}. The derivation is limited to ocean cloud scenes.

High values of the aerosol DRE over clouds are typically found in areas with thick smoke plumes overlying a marine stratocumulus cloud deck in the boundary layer. This is illustrated in Figure 1, where the aerosol DRE is quantified over the Atlantic during three consecutive days (5,6,7 August 2016). It shows the synoptic situation during the satellite overpasses (13:30 local time), using RGB images from MODIS, mainly illustrating the position of the clouds. The clouds in this region are typically extensive fields of marine stratocumulus cloud decks in the boundary layer. The DRE (in Wm^{-2}) is overplotted, showing the places where smoke over the clouds absorbs solar radiation. Overplotted on this are backtrajectories of air parcels ending on 7 August 2016 at 500 m, 1500 m and 3000 m altitude, respectively, over Ascension Island, a small island at 8.0° S, 14.4° W, computed using the HYSPLIT model [RD5]. The position of the air parcel during the satellite overpasses is given exactly by the stars on each day. They show that the plume of smoke that absorbs the large amount of radiation passes over the Atlantic in a few days, in a layer at around 1500–2000 m altitude. Only this layer was over the continent at ground level until 2 August 2016, lifted to about 2000 m, and slowly descending to 1500 m over Ascension Island. The other levels are not clearly connected to the position of the smoke plume.

Another illustration is given below using SCIAMACHY data.

6.2 Heritage

The aerosol DRE was originally developed using SCanning Imaging Absorption spectroMeter for Atmospheric CHartographY (SCIAMACHY) data [RD4]. SCIAMACHY was a spectrometer on the Environmental Satellite (Envisat) launched in 2002 into a polar orbit with an Equator crossing time of 10:00 LT for the descending node. It had the unique capability to observe a contiguous reflectance spectra from 240 to 1750 nm at a spectral resolution of 0.2 to 1.5 nm. This contains 92% of the energy of the solar spectrum and was used to capture the absorption by UV-absorbing smoke over the Atlantic. SCIAMACHY acquired data alternately in nadir and limb mode, producing data blocks called 'states',approximately 960×480 km^2 in size.

The use of SCIAMACHY data is illustrated in Figure 2. It shows the DRE over the southeast Atlantic ocean on 13 August 2006, when a huge smoke plume is overlying the marine boundary layer stratocumulus cloud deck. The cloud deck is illustrated using an RGB image from MERIS, an imager also on EnviSat. For one SCIAMACHY pixel, where the aerosol DRE is very high, 124 Wm^{-2}, the measured scene reflectance spectrum is shown in red, while the equivalent cloud scene refeflectance spectrum for that scene when no smoke had been present is given blue. The red line represents the spectrum of the aerosol polluted cloud spectrum, while the blue line represents the unpolluted cloud spectrum, which was simulated using a radiative transfer model scheme. The difference between these spectra is due to radiation absorption by aerosols (indicated in yellow). Clearly, the absorption is largest in the UV and disappears in the SWIR. The states are indicated as white rectangles. Over clouds, where no smoke present, the aerosol DRE is low. If no clouds are present, or over land, the aerosol DRE is not computed.

The vertical extend of the smoke and cloud deck can be visualised using lidar data from Calipso on CALIOP. The CALIOP track on 13 August 2006 around 01:25 UTC is shown in Figure 2 as the yellow line. This overpass is very close to SCIAMACHY overpass in space, and about eight hours before the SCIAMACHY measurements. The night time measurements around 01:25 UTC from the Calipso lidar are shown in Figure 3 as a curtain plot, showing the total attenuated backscatter at 532 nm as a function of altitude along the track shown in Figure 2.

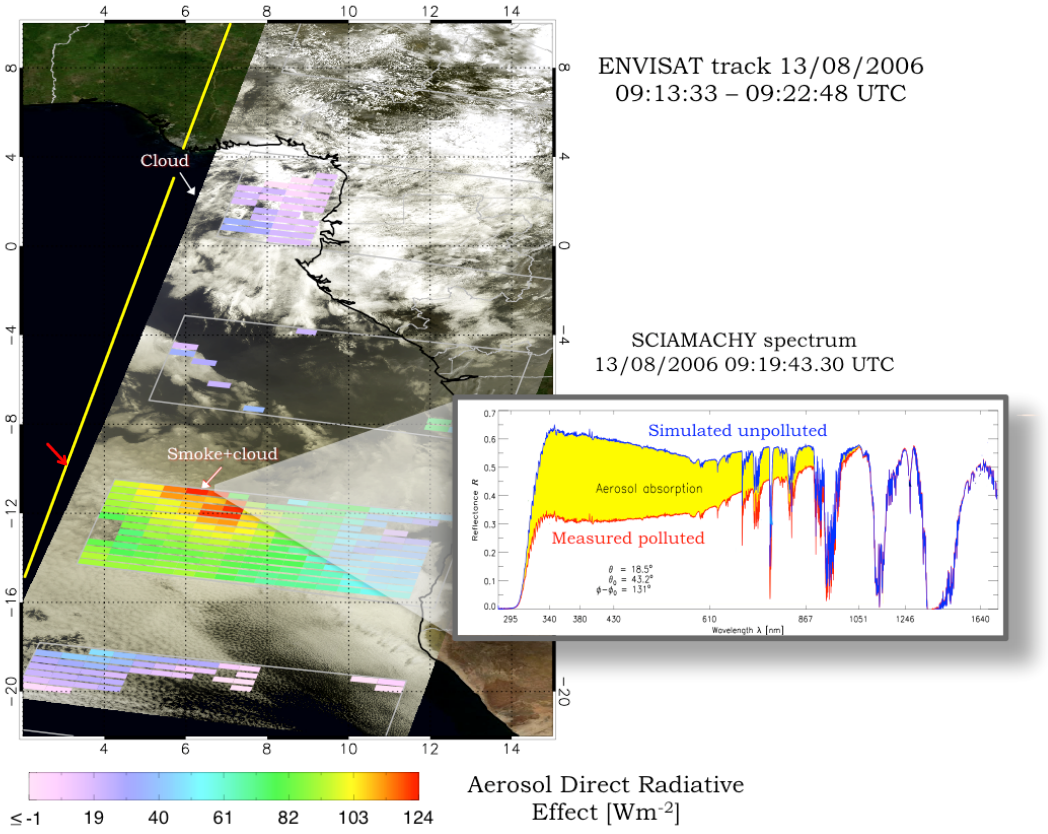

Figure 2: MERIS RGB image on 13 August 2006 around 9:19 UTC, with the SCIAMACHY aerosol DRE over clouds overplotted. The SCIAMACHY spectrum for the pixel with the highest DRE is given in the inset in red, while the equivalent spectrum for the same scene with the same cloud but without the overlying aerosols is given in blue. The CALIOP track around 1:25 UTC is given by the yellow line. The total attenuated backscatter along this track is given in Figure 3. The location of the red arrow corresponds with the location of the red arrow in Figure 3.

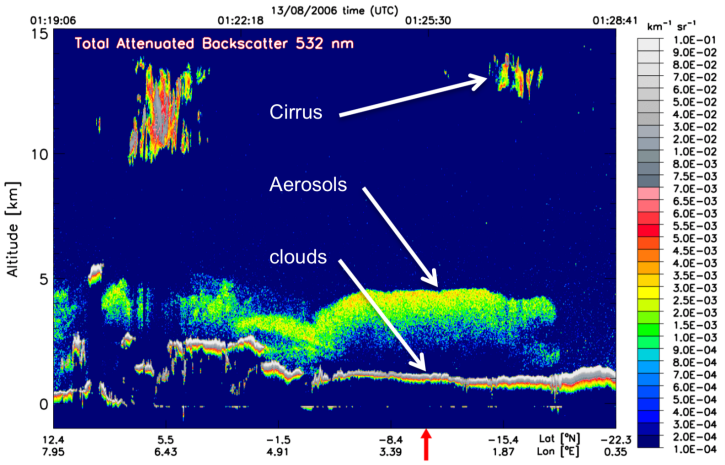

Figure 3: Total attenuated backscatter signal from Calipso in CALIOP, along the yellow track shown in Figure 2. The color scale is such that generally grey colors correspond with clouds, green to red colors correspond with aerosol layers, and blue colors corrspond to clean air. The location of the red arrow corresponds with the location of the red arrow in Figure 2, which is the position of the closest proximity of the CALIOP track to the SCIAMACHY pixel with the highest DRE.

This illustrates the vertical location of the cloud (top) and aerosol plume (top). Note that the lidar beam does not penetrate the cloud, and also saturates in the smoke layer, and the high backscatter signals only indicate the location of the top of the layers, and cannot show the bottom of the layers. Whether the aerosol plume touches the cloud layer or not remains unresolved [RD6].

After SCIAMACHY stopped producing data is 2012, a DRE retrieval was developed based on OMI and MODIS reflectances [RD7], which together cover the UV to SWIR spectral range. This requires careful combining the reflectance spectra from OMI, with a footprint of 15 $\times$ 24 km^2 at nadir, and MODIS reflectances, which have spatial resolutions of 250 – 500 m. This is described in [RD7] and in section 6.3.4.

6.3 Algorithm description

6.3.1 Theory

The radiative effect of an atmospheric constituent can be defined as the net broadband irradiance change $\Delta\mathscr{E}$ at a certain level with and without the forcing constituent, after allowing for stratospheric temperatures to readjust to radiative equilibrium, but with tropospheric and surface temperatures and state held fixed at the unperturbed values. For tropospheric aerosols as the forcing agent, stratospheric adjustments have little effect on the radiative forcing and the instantaneous irradiance change at the TOA can be substituted:

$$\Delta\mathscr{E}_{\text{aer}}^{\text{TOA}} = \mathscr{E}_{\text{with aer}}^{\text{net}} - \mathscr{E}_{\text{without aer}}^{\text{net}}, \tag{1}$$

where $\mathscr{E}^{\text{net}}$ is the net irradiance, defined as the difference between the downwelling and upwelling shortwave irradiances at the TOA, $\mathscr{E}^{\text{net}} = \mathscr{E}^{\downarrow} - \mathscr{E}^{\uparrow}$. Furthermore, the extinction optical thickness of biomass burning aerosols decreases strongly with increasing wavelength. Therefore, biomass burning aerosols do not significantly interact with the longwave (terrestrial) radiation, so the net broadband irradiance can be substituted by the net shortwave irradiance. At the TOA the shortwave downwelling irradiance is the total incoming solar irradiance $\mathscr{E}_0$ for any scene, and $\mathscr{E}^{\downarrow}$ can be eliminated. Consequently, for aerosols overlying a cloud the direct radiative effect is given by

$$\Delta\mathscr{E}_{\text{aer}}^{\text{TOA}} = \mathscr{E}_{\text{cld}}^{\uparrow\ \text{TOA}} - \mathscr{E}_{\text{cld+aer}}^{\uparrow\ \text{TOA}}, \tag{2}$$

where $\mathscr{E}_{\text{cld}}^{\uparrow\ \text{TOA}}$ is the upwelling irradiance at the TOA for an aerosol-unpolluted cloud scene and $\mathscr{E}_{\text{cld+aer}}^{\uparrow\ \text{TOA}}$ is the upwelling shortwave irradiance for an aerosol-polluted cloud scene. By equation (2), if energy is absorbed in the atmosphere by the aerosols, the direct radiative effect is positive.

The aerosol DRE over clouds is determined from shortwave hyperspectral measurements of passive spectro(radio)meters, using measured reflectances of cloud scenes. The primary satellite product here is the Earth reflectance $R(\lambda)$, measured in the shortwave domain as a function of wavelength at a high spectral resolution. The monochromatic reflectance $R(\lambda)$ is defined as the quotient of the upwelling monochromatic radiance $I(\lambda)$ and the downwelling monochromatic solar irradiance $E_0(\lambda)$:

$$R(\lambda) = \frac{\pi I(\lambda)}{\mu_0 E_0(\lambda)}, \tag{3}$$

where μ_0 is the cosine of the solar zenith angle θ_0 and $\mu_0 E_0$ is the solar irradiance incident on a horizontal surface unit at TOA. $R(\lambda)$ is also computed by the RTM at discrete wavelengths. Below, R and all other quantities refer to the TOA.

The monochromatic irradiance $E(\lambda)$ of the reflected radiation can be found by integrating $I(\lambda)$ over the entire hemisphere, weighted by μ, where μ is the cosine of the viewing zenith angle θ. Substituting equation (3) and using polar coordinates (θ, ϕ):

$$E(\lambda) = \frac{\mu_0 E_0(\lambda)}{\pi} \int_0^{2\pi}\int_0^1 R(\lambda;\mu,\phi;\mu_0,\phi_0)\mu\,\mathrm{d}\mu\mathrm{d}\phi, \tag{4}$$

where ϕ_0 and ϕ are the azimuth angles of the solar and viewing directions, respectively. Similarly, the (local) plane albedo A for a scene is defined as the integral of $R(\lambda)$ over the entire hemisphere [RD8]:

$$A(\lambda,\mu_0) = \frac{1}{\pi} \int_0^{2\pi}\int_0^1 R(\lambda;\mu,\phi;\mu_0,\phi_0)\mu\,\mathrm{d}\mu\mathrm{d}\phi. \tag{5}$$

By substituting equation (5) in (4) and integrating over wavelength in the shortwave (SW) domain, equation (2) becomes

$$\Delta\mathscr{E}_{\rm aer}(\mu_0) = \int\limits_{\rm SW} \mu_0 E_0(\lambda)\,(A_{\rm cld}(\lambda,\mu_0) - A_{\rm cld+aer}(\lambda,\mu_0))\,{\rm d}\lambda. \tag{6}$$

6.3.2 Differential Aerosol Absorption technique

The aerosol DRE over clouds is determined using RTM results for the first term in equation (6), $A_{\rm cld}$, and measurements of the reflectance $R(\lambda)$ for the second term, $A_{\rm cld+aer}$. From the RTM results, the plane albedo $A_{\rm cld}$ can be determined from integration of the reflectances in all directions. However, from a satellite instrument only the reflectance in the viewing direction is known. Therefore, the plane albedo for this scene, $A_{\rm cld+aer}$, must be estimated. A measure for the angular distribution of the reflected radiation for a scene is the anisotropy factor $B(\lambda,\mu_0) = R/A$. The anisotropy factors are assumed to be unchanged by the aerosols over the clouds nad therefore equal for the aerosol-unpolluted and aerosol-polluted cloud scenes, $B_{\rm cld} = B_{\rm cld+aer}$.

Then, equation (6) can be rewritten and the instantaneous aerosol direct radiative effect over clouds $\mathrm{DRE}_{\rm aer}$ can be defined as the net shortwave irradiance change at the TOA:

$$\mathrm{DRE}_{\rm aer} = \Delta\mathscr{E}_{\rm aer}(\mu_0) = \int\limits_{SW} \frac{(R(\lambda)_{\rm cld} - R(\lambda)_{\rm cld\,+\,aer})\,\mu_0 E_0(\lambda)}{B(\lambda,\mu_0)_{\rm cld}}\,{\rm d}\lambda + \varepsilon, \tag{7}$$

where $R(\lambda)_{\rm cld}$ is a simulated aerosol-free cloud reflectance, representative for the measured scene with the aerosols removed. The aerosol DRE follows from the integration of the radiance difference between the simulated aerosol-free cloud scene and measured aerosol polluted cloud scene over the solar spectrum, hence the term differential aerosol absorption was coined. The wavelength integration limits in Eq. 7 were 240 and 1750 nm for the contiguous SCIAMACHY reflectance measurements. In case of combined OMI and MODIS reflectances, the integration limits are from the start of OMI measurements (about 270 nm) to the first of the MODIS channels that are used to invert cloud parameters (1246 nm), where the aerosol absorption is assumed to have become negligible. ε represents all the instrument and retrieval errors of a single measurement, due to the assumptions described above and the measurement uncertainties. These will be quantified in section 9.

An illustration of the DAA technique is given in Fig. 4. The first step is the selection of suitable scenes, i.e. the selection of scenes with clouds; see above. To ensure the selection of (low-level) water clouds, only pixels with a cloud pressure larger than a threshold (e.g. 800 hPa) are selected. Step two is the determination of a measured scene reflectance spectrum. For SCIAMACHY this was trivial; the combination of OMI and MODIS reflectances is treated in Sect.??. Step three is the retrieval of the cloud optical thickness (COT) and cloud droplet effective radius $r_{\rm eff}$, using the SWIR part of the reflectance determined in step two, (e.g. $R_{1.2\mu{\rm m}}$ and $R_{2.1\mu{\rm m}}$) and tabulated SWIR reflectances. The fourth step is the simulation of the cloud scene reflectances in the UV, visible and SWIR part of the spectrum. This forward step is also performed using a LUT as before, which contains reflectances at 18 wavelengths from 295 nm to 2130 nm, see section 6.3.6. Once the simulated and measured cloud scene reflectances are available, the DRE is computed in step five, using Eq. 7 and a measured or reference solar irradiance spectrum $E_0(\lambda)$.

6.3.3 Water cloud selection

The pixels are filtered for cloud fractions lower than 0.2 and cloud pressure larger than 800 hPa, using the OMI O2-O2 cloud product.

6.3.4 Measured reflectance extraction

After selection of suitable cloud pixels, a hyperspectral reflectance spectrum is constructed using collocated OMI and MODIS/Aqua pixels. Spectrally, OMI overlaps with MODIS at 459–479 nm (central wavelength 469 nm), which can be used to match the OMI reflectances in the visible channel and the MODIS reflectance in band 3. Spatially, the overlap is more complicated, since the OMI footprint is not uniquely defined due to the use of a polarisation scrambler. The polarisation scrambler projects four depolarized beams onto the detector CCD, which are slightly shifted with respect to each other, and therefore only the central point of the OMI footprint is uniquely defined. Furthermore, since the optics of OMI contain no moving mirror, but projects the incoming radiation onto the CCD detector array directly during a 2 s interval, the spatial response function of the OMI footprints is not box-shaped, but rather Gaussian-shaped in two dimensions. 74 % of the radiance

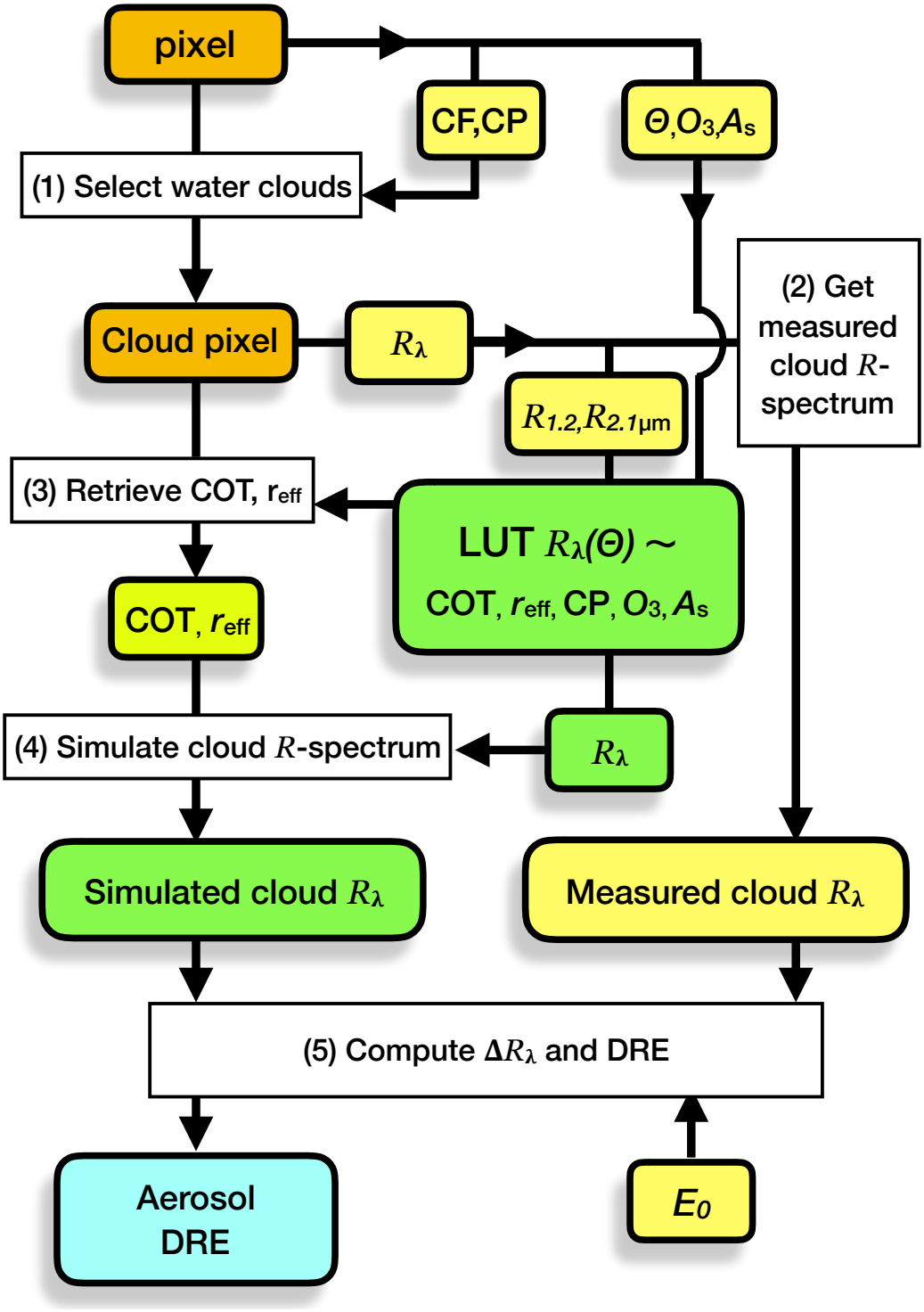

Figure 4: Flow diagram for the Differential Aerosol Absorption technique. Yellow boxes contain pixel products, green boxes contain simulated quantities, the yellow/green box is a retrieval for the cloud pixel and the light blue box is the end product. Θ represents the geometry of the measurements, E_0 is the irradiance spectrum, R_λ is the reflectance (spectrum), CF is cloud fraction, CP is cloud pressure, COT is cloud optical thickness, r_{eff} is cloud droplet effective radius, O_3 is the ozone profile, and A_s is the surface albedo.

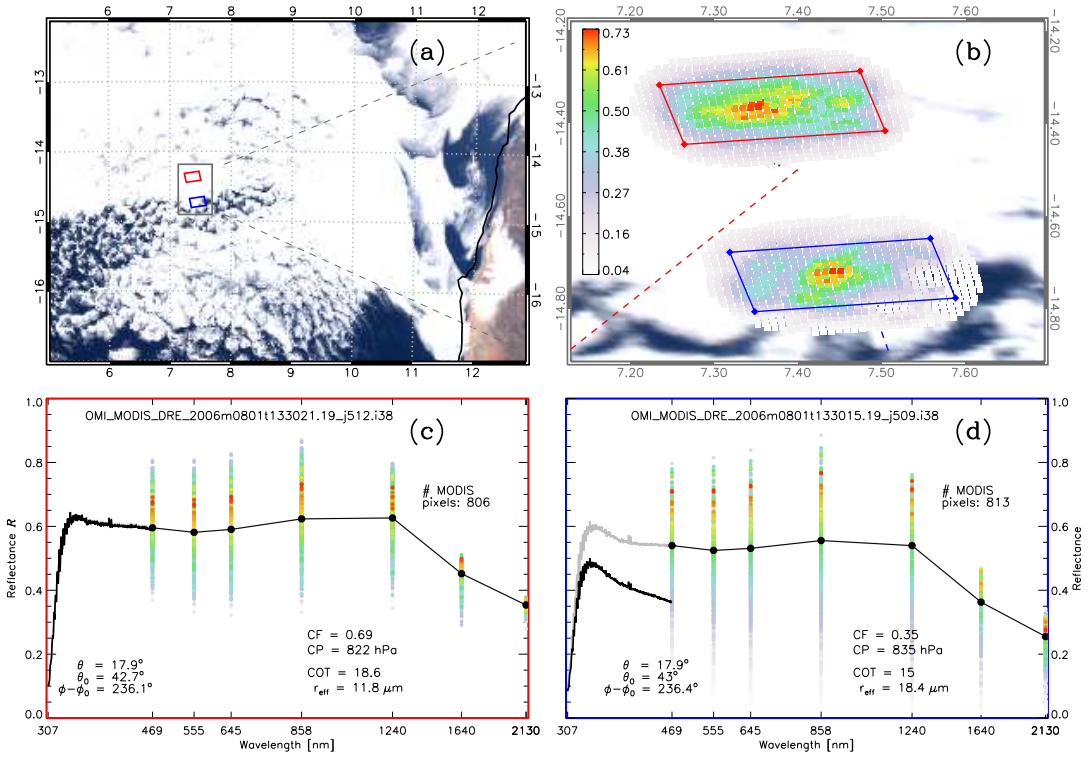

Figure 5: Illustration of the computation of the Aerosol DRE from a combination of one OMI pixel and collocated MODIS pixels. (a) Overview of a stratocumulus cloud deck over the southeast Atlantic Ocean using MODIS RGB and two selected OMI pixels in red and blue on 1 August 2006. (b) Close-up of the two selected OMI pixels, with collocated high-resolution MODIS pixels, coloured by their intensity, which is determined by the MODIS reflectance, convolved with the OMI pixel point spread function that is used to weight the contribution of the individual MODIS pixels. (c) Shortwave spectrum from the red OMI pixel, acquired at 13:30:21 UTC, combined with the average MODIS reflectance (both in black), acquired around 13:14:15 UTC. The coloured dots indicate the weight of the individual MODIS pixels. (d) Shortwave spectrum of the blue OMI pixel, acquired at 13:30:15 UTC (black), and the average of the MODIS pixels, acquired around 13:14:09 (black). The grey curve indicates the OMI spectrum after scaling with the average MODIS spectrum.

received at a detector pixel is from within the corner coordinates, the rest of the signal is from outside the pixel corner coordinates. The OMI field of view was analyzed in detail in [RD9] and [RD10]. A 2D-Gaussian shape is used here to average MODIS reflectances across the OMI pixel, favoring pixels near the OMI center and allowing for overlapping ground pixels.

The projections of radiation are slightly different in the two OMI UV channels and the OMI visible channel, resulting in slightly different ground pixels and wavelength grids, but these have not been accounted for. All computations were performed and reported relative to the wavelength grid and ground pixels of the OMI visible channel.

Two examples of OMI pixels tiled with MODIS pixels are shown in Fig. 5. Figure 5a shows an overview of the situation: a broken cloud field over the southeast Atlantic Ocean, west of Africa, with two OMI pixels, one in the stratocumulus cloud deck (red), and one at the cloud edge (blue). Figure 5b shows the MODIS pixels that are collocated with the OMI pixels, colored by their weight in the averaging of the reflectance, which is the reflectivity convolved with the Gaussian function. Clearly, points close to the OMI pixel center are favored, but also pixels beyond the corner coordinates contribute to the radiation in the pixel. The cloud structure clearly has a large influence on the contributing pixels.

Figure 5c shows the combined OMI-MODIS reflectance of the fully cloudy scene (red), while Fig. 5d shows the combined OMI-MODIS reflectance of the broken cloud scene (blue). Clearly, there is a mismatch between OMI and MODIS for the broken cloud scene, which is caused by changes in the reflectance due to changes in the cloud fraction in the OMI footprint. The average reflectance of the scene has changed during the 15 minutes between overpasses of Aura and Aqua. The OMI/FRESCO effective CF was 0.69 in the red pixel, and 0.35 in

the blue pixel. Fifteen minutes earlier, during the MODIS overpass, the geometric MODIS CF was around 0.99 and 0.98, respectively. Note that effective cloud fraction is generally lower than geometric cloud fractions. In order to get a contiguous reflectance spectrum, the average reflectance during the MODIS overpass is taken and OMI was scaled to match the MODIS average reflectance at 469 nm. Scaling MODIS to OMI seemed obvious at first, to have all parameters at the OMI grid and time. However, this resulted in very noisy data, because scaled MODIS reflectances resulted in flawed cloud parameter retrievals at longer wavelengths and the accuracy of the DRE over clouds depends strongly on the accuracy of the cloud parameters. The derivation of cloud parameters is treated below.

6.3.5 Cloud retrieval

In the current implementation, the MODIS reflectances at 1.2 μm and 2.1 μm are used to derive cloud droplet effective radius and cloud optical thickness, following [RD11]. Using wavelengths in the SWIR, instead of the visible, avoids biases of cloud parameters due to absorption by overlying aerosols [RD12]. The cloud parameters retrieved in this way have a larger uncertainty, but can be used for scenes with overlying aerosols [RD4]. Note that the MODIS reflectance at 1.6 μm is not used for the cloud retrieval, because of the large number of bad and dead pixels in the MODIS/Aqua detector [RD13]. The cloud droplet effective radius and cloud optical thickness are used to construct an aerosol-free cloud scene reflectance spectrum using RTM simulations ($R(\lambda)_{\rm cld}$ in Eq. 7.) Since the retrieval of the DRE is depending so much on the correct cloud parameters and subsequent scene reflectance, the average MODIS reflectances have to be taken as a basis, and OMI reflectances have to be scaled to MODIS. The cloud optical thickness and cloud effective radii are shown in Fig. 5, representing the clouds in the two OMI pixels during MODIS overpass.

6.3.6 Cloud spectrum modelling

The fourth step is the simulation of the cloud scene reflectances in the UV, visible and SWIR part of the spectrum. This step is performed using the cloud pressure and effective cloud droplet radius found before, and extracting the reflectances at 18 spectral points from 295 nm to 2130 nm for these cloud parameters, using the same LUT as before, see Table 1.

Table 1: Spectral cloud reflectance LookUp Table nodes

Parameter	Nodes								
wavelength λ [nm]	295	310	320	330	340	380	430	469	555
	610	645	858	867	1051	1240	1246	1640	2130
cloud optical thickness $\tau_{\rm cld}$	2	4	8	12	16	20	24	32	48
droplet size $r_{\rm eff}$ [μm]	3	4	6	8	12	16	20	24	
cloud base height $z_{\rm cld}$ [km]	0	1	4	8	12				
total O_3 column Ω [DU]	267	334	401						
surface albedo $A_{\rm s}$	0	0.5	1						
droplet size eff. variance $v_{\rm eff}$	0.15								
number of θ_0, θ, $\phi - \phi_0$	14	14	19						

6.3.7 Direct radiative effect computation

The final step is the derivation of the direct radiative effect using the spectral difference between the simulated and measured spectrum. The reflectance differences at the 18 wavelength nodes are interpolated and multiplied using a high resolution irradiance spectrum, to find the radiance difference This is then divided by the anisotropy factor for the cloud scene and interpolated from the UV to SWIR, see Eq. 7. The last step is illustrated in Fig. 6.

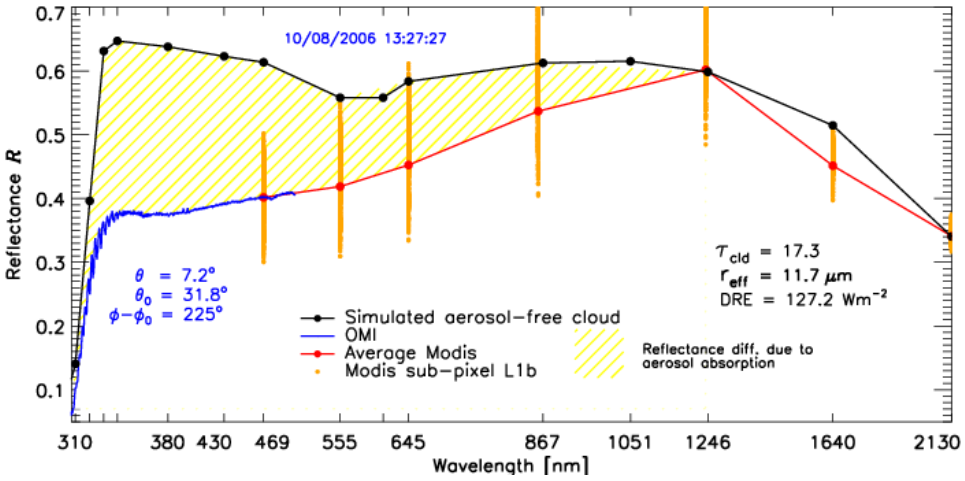

Figure 6: The differential Aerosol Absorption technique illustrated with a combined OMI and MODIS spectrum. In blue the spectrum measured by OMI is given for the pixel indicated by the blue arrow in Fig. 7, and in red the MODIS average spectrum for this pixel. The black solid line shows the simulated aerosol-free cloud spectrum computed with an RTM for the OMI pixel. The yellow shaded part shows the reflectance difference for this pixel. The orange dots show the range of reflectance values at the different MODIS channels in this OMI pixel, the red dot is the weighted average reflectance.

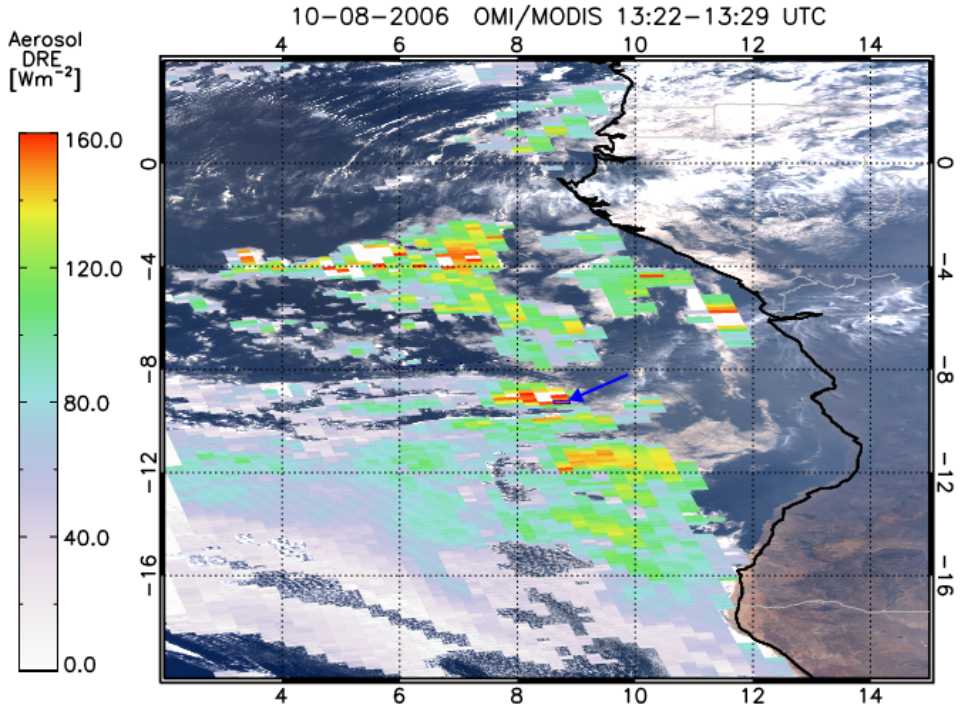

Figure 7: Instantaneous aerosol direct radiative effect (DRE) over clouds on 10 August 2006 from a combination of OMI and MODIS reflectances, overlaid on a MODIS RGB image. The reflectance spectrum of the pixel indicated by the blue arrow is given in Fig. 6.

7 Feasibility

As mentioned in section 6 the satellite derived DRE is a combination of measurements by the satellite instruments OMI and MODIS. Combining measurements from these two instruments is a computationally very demanding task, and the area for which the aerosol DRE was computed is small, only a large part of the southeast Atlantic Ocean is covered, for all other areas the product is currently not available, see Fig. 8. However, the computation of the DRE from these spectra is dependent on a LUT retrieval, which is a common retrieval technique, which is suitable for any retrieval in Near-Real Time (NRTI). If spectra are available from an instrument which covers the UV to SWIR, DRE retrieval in NRTI is feasible.

8 Availability

Currently, the OMI DRE is available over the southeast Atlantic only, from 2005 for the biomass burning season, 1 June to 31 October. It can be freely downloaded from the Tropospheric Emission Monitoring Internet Service (TEMIS) website: *https://www.temis.nl/*

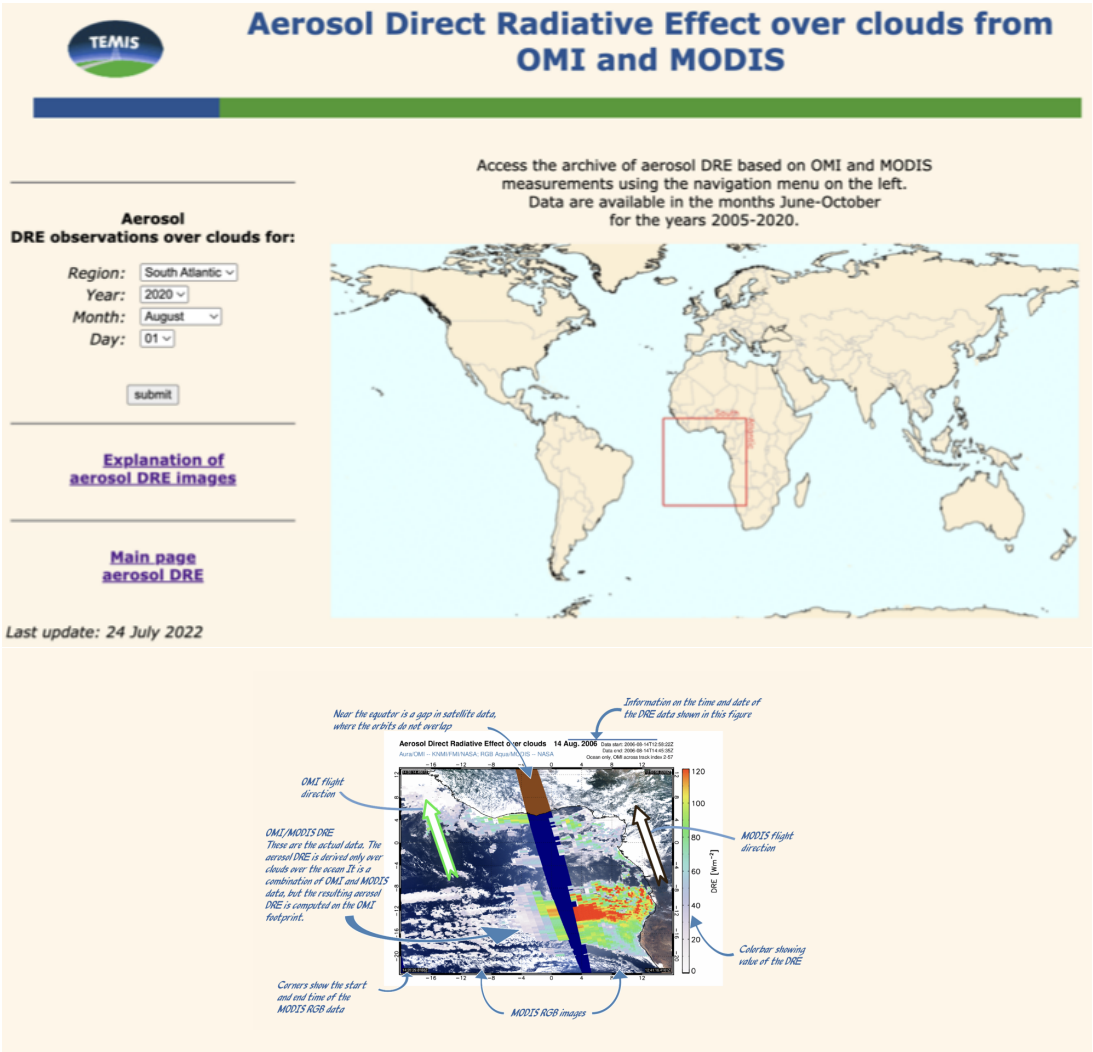

Figure 8: OMI DRE TEMIS page on *www.temis.nl*, showing the region with available data and an explanation of the images.

9 Error Analysis

The error in the DRE retrievals was extensively discussed in [RD4] and [RD7]. Here, a number is discussed, using both SCIAMACHY spectra and OMI-MODIS spectra, to show the error sources and accuracy of the DRE retrieval.

9.1 Clouds

9.1.1 Unpolluted cloud spectra accuracy assessment

The LUTs described in section 6.3.6 provide an independent calibration tool for satellite measurements of unpolluted (aerosol-free) cloud reflectance spectra. An example of a modelled and a measured unpolluted cloud reflectance spectrum is shown in Figure 9, using a measurement from SCIAMACHY. The measured cloud reflectance spectrum on 14 August 2006 at 10:30:04 UTC over the South-Atlantic Ocean is shown in various colours, according to different integration times (IT) of SCIAMACHY. Parts of the spectrum that were sampled with an IT of 0.25 s, and co-added, are shown in red, parts that were sampled with an IT of 0.5 s, and co-added, are shown in green, and parts that were sampled with an IT of 1 s are shown in blue. The entire spectrum has an IT of 1 s. The absence of UV-absorbing aerosols was confirmed by a negative AAI value of -0.8. The FRESCO cloud fraction and cloud pressure were 0.7 and 856 hPa for this scene, respectively, indicating a marine low level cloud. The cloud optical thickness and droplet effective radius for this scene were 14.3 and 15.4 μm, respectively. The simulated unpolluted cloud reflectance spectrum using these parameters is shown in black. The difference between the simulated and measured reflectance spectra is plotted in the lower panel of Figure 9, and shows that the difference is in general very small (< 0.015) for this scene. The differences are well within the uncertainty of SCIAMACHY's reflectance measurements of about 3%. Apparently, an unpolluted cloud reflectance spectrum can be accurately extrapolated from the SWIR to the visible and the UV.

The differences between the modelled and measured spectra are caused by measurement uncertainties and the errors in the retrieval of the cloud optical thickness and effective droplet size. Minor causes are

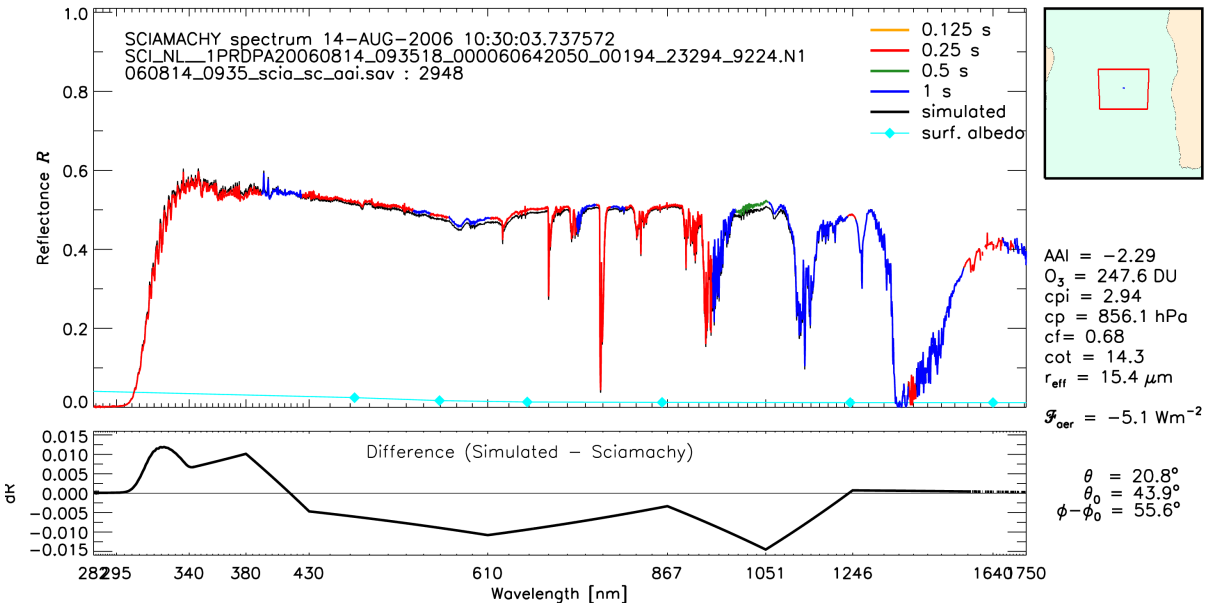

Figure 9: Simulated (black) and measured reflectance spectra of an aerosol-unpolluted water cloud scene on 14 August 2006 at 10:30:04 UTC at different ITs: 0.25 s (red), 0.5 s (green) and 1 s (blue). The absence of absorbing aerosols above the clouds was ensured by a negative value of the AAI of -0.8. This scene was characterised by a cloud phase index of 3, a cloud fraction of 0.7 and a cloud pressure of 856 hPa, indicating a low level marine cloud. The retrieved $\tau_{\rm cld}$ for this scene was 14.3, the $r_{\rm eff}$ was 15.4 μm. The simulated cloud spectrum for these cloud parameters, the scene geometry and a total ozone column of 248 DU, is shown in black. The modelled surface albedo is shown in cyan. The reflectance difference between the simulated and measured cloud scene is shown in the lower panel. The sampled scene is the blue spot in the middle of the red box over the South-Atlantic Ocean as shown in the inset.

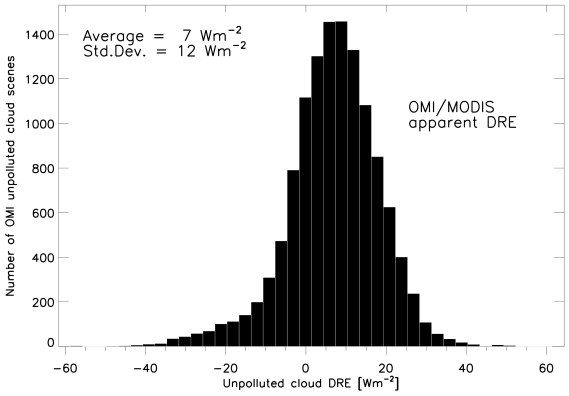

Figure 10: Frequency distribution of the apparent aerosol effect of all OMI aerosol-unpolluted marine water cloud scenes in June–Sept. 2006 over the southeast Atlantic Ocean (20° S to 10° N; 10° W to 20° E). The OMI-MODIS DRE for each pixel with OMI AI<0, CF>0.3 and CP>800 hPa was considered. The offset (apparent DRE) for these pixels is 7 Wm^{-2}, which is taken as the bias of the OMI-MODIS DRE method. The standard deviation of the DRE for these unpolluted scenes is 12 Wm^{-2}, which is a measure of the random error of the DRE.

interpolation errors in the LUT and possibly scattering by aerosols in the scene that cannot be distinguished from clouds. The latter errors are random, but SCIAMACHY measurement and $\tau_{\rm cld}$ and $r_{\rm eff}$ retrieval errors may be systematic. The presented case is typical for measurements of unpolluted water cloud spectra. In the case of SCIAMACHY measurements, the uncertainties due to misrepresentation of cloud reflectances was estimated at 7 Wm^{-2}.

For OMI-MODIS measurements this error is larger, due to the low spectral resolution of the measurements beyond 500 nm. It was tested by comparing measured aerosol-free cloud spectra $R_{\rm cld}^{\rm meas}$ to simulated spectra $R_{\rm cld}^{\rm sim}$ for scenes that are screened for absorbing aerosols, to ensure unpolluted scenes. Figure 10 shows the aerosol DRE for aerosol-free cloud scenes in June to August 2006. Only scene were considered with an OMI O_2-O_2 effective cloud fraction larger than 0.3 to ensure a sufficiently clouded scene, and an OMI O_2-O_2 cloud pressure higher than 800 hPa, to exclude ice clouds. To ensure the absence of absorbing aerosols an OMI with an OMAERO AI v.1.1.1 smaller than 0, following [RD14]. The average difference in DRE between the simulated and real scenes was about 7 Wm^{-2}, was previously considered a systematic error of the differential absorption technique for aerosol-free scenes. However, the exact threshold for AI to exclude aerosols is not unambiguous, and a test with different AI thresholds showed that the average DRE for OMI-MODIS aerosol-free cloud scenes is reduced to only 1 Wm^{-2} when scene with AI smaller than -1.0 are considered. Therefore, a bias due to cloud modeling may be much smaller than the 7 Wm^{-2} shown in Fig. 10.

The standard deviation for the apparent DRE between simulated and real spectra shown in Fig. 10 was 12 Wm^{-2}. The standard deviation was not sensitive to a change in AI threshold, and can be considered a random error.

9.1.2 Polluted cloud spectra accuracy assessment

To fully understand the processes involved in the observed reflectances, model calculations were performed which simulate not only the unpolluted cloud scene, but also a polluted cloud scene. The cloud layer was simulated in a 1 km thick layer with variable optical thickness, simulated as before.

A Mie model for smoke was used with a refractive index at 550 nm of $1.54 - 0.018i$. This number was found for aged smoke during the SAFARI 2000 campaign [RD15] and was used for all wavelengths longer than 550 nm. However, for the UV spectral region the imaginary refractive index was modified in line with recent studies that have indicated that biomass burning aerosols are characterised by a significant fraction of organic carbon (OC) [RD16, RD17], which is produced mainly by incomplete combustion processes. The light absorbing efficiency of OC increases strongly with decreasing wavelength in the UV. In contrast, aerosols dominated by black carbon (BC) have wavelength independent refractive indices (‘gray’ aerosol). These aerosols are found more in industrial waste products, where combustion processes have been optimised. The wavelength dependence of the aerosol absorption is expressed by the absorption Ångström exponent,

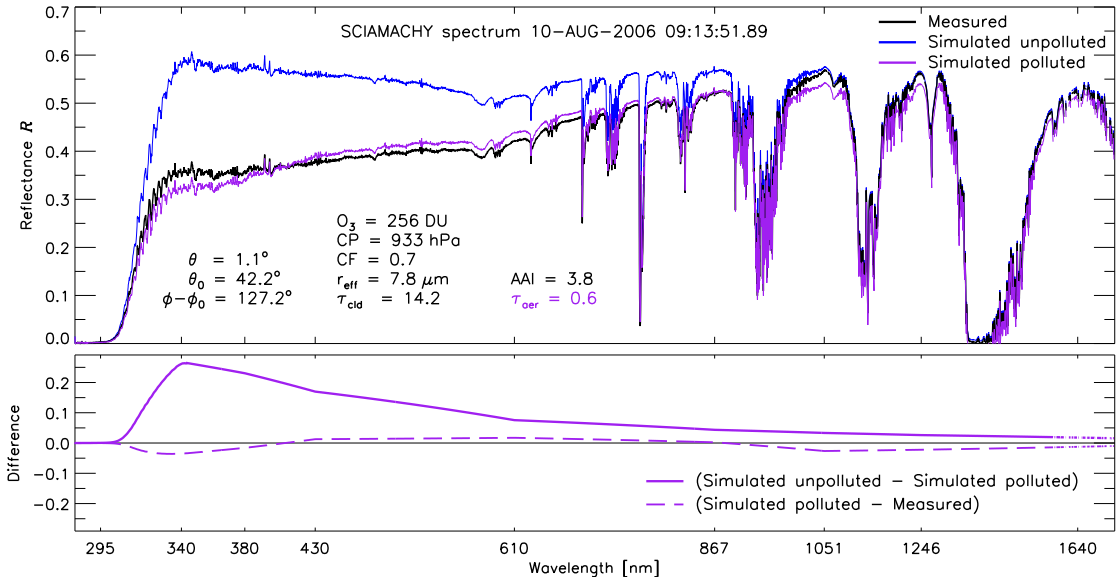

Figure 11: Top panel: modelled aerosol-polluted cloud reflectance spectrum (purple), together with the measured SCIAMACHY scene reflectance (black) and the modelled equivalent aerosol-unpolluted cloud reflectance spectrum (blue) on 10 August 2006 at 09:13:51.89 UTC. The optical thickness of the model aerosol layer τ_{aer} was 0.6 at 550 nm. Bottom panel: Difference between the simulated and measured aerosol-polluted cloud reflectance spectra (dashed purple) and the difference between the simulated unpolluted and polluted cloud reflectance spectra (solid purple).

which is different for different types of aerosols. The absorption Ångström exponent for African biomass burning aerosols from SAFARI 2000 observations was found to be around 1.45 in the spectral region from 325 to 1000 nm [RD17, RD18]. Satellite observations from OMI proved better fitted with aerosol models that had absorption Ångström exponents from 2.5 to 3 in the UV [RD19]. The absorption Ångström exponent for the smoke model used here was 2.91 in the UV. This fitted the wavelength dependence of the reflectance spectrum well when applied in a model scene of smoke and clouds, see Figure 11. A bi-modal log-normal size distribution model was used, based on the 'very aged' (5 days) biomass plume found over Ascension Island during SAFARI 2000 [RD15]. The geometric radii for this haze plume used in the simulations here were $r_{\text{c}} = 0.255$ μm and $r_{\text{f}} = 0.117$ μm for the coarse and fine modes, with standard deviations $\sigma_{\text{c}} = 1.4$ and $\sigma_{\text{f}} = 1.25$, respectively. The fine mode number fraction was 0.9997.

The aerosol extinction optical thickness τ_{aer} of the aerosol layer was fitted so that the total irradiance change of the modelled scene matched that of the measured scene. For a scene on 10 August 2006, at 09:13:52 UTC this yielded a τ_{aer} of 0.6 at 550 nm, see Figure 11. The reflectance spectrum of this modelled scene is shown by the purple curve, while the measured reflectance spectrum is given in black and the modelled unpolluted cloud reflectance spectrum in blue. The differences between the modelled aerosol-polluted cloud scene and the measured and modelled unpolluted cloud scenes are given in the lower panel. The simulation follows the measurements closely over most of the spectral region, confirming the wavelength dependence of the smoke refractive index. Below about 400 nm the slope of the reflectance spectrum is slightly overestimated, so the absorption Ångström exponent should probably be smaller in this spectral region for this scene. The polluted cloud scene is analysed to assess the errors involved in adding aerosols to a cloud scene.

9.1.3 Errors in cloud and aerosol optical thickness

The effects of varying AOT and varying COT on the aerosol DRE over clouds are illustrated in Figure 12a for an AOT between 0.1 and 1, and a COT of 8 and 16, with cloud effective radii of 8 and 12 μm. The solar zenith angle (SZA) in the simulations shown was 30°, the relative azimuth angle (RAZI) was 0° and two viewing zenith angles of 10 and 60° are shown, which span a typical range of viewing angles for OMI. The figure clearly shows a linear relationship between AOT and DRE, with an increasing aerosol DRE with increasing AOT, as expected. However, as known, the increase in DRE with AOT depends mainly on the COT of the underlying clouds. With larger COT, the amount of light at TOA increases, and the amount of absorption by the aerosols above the

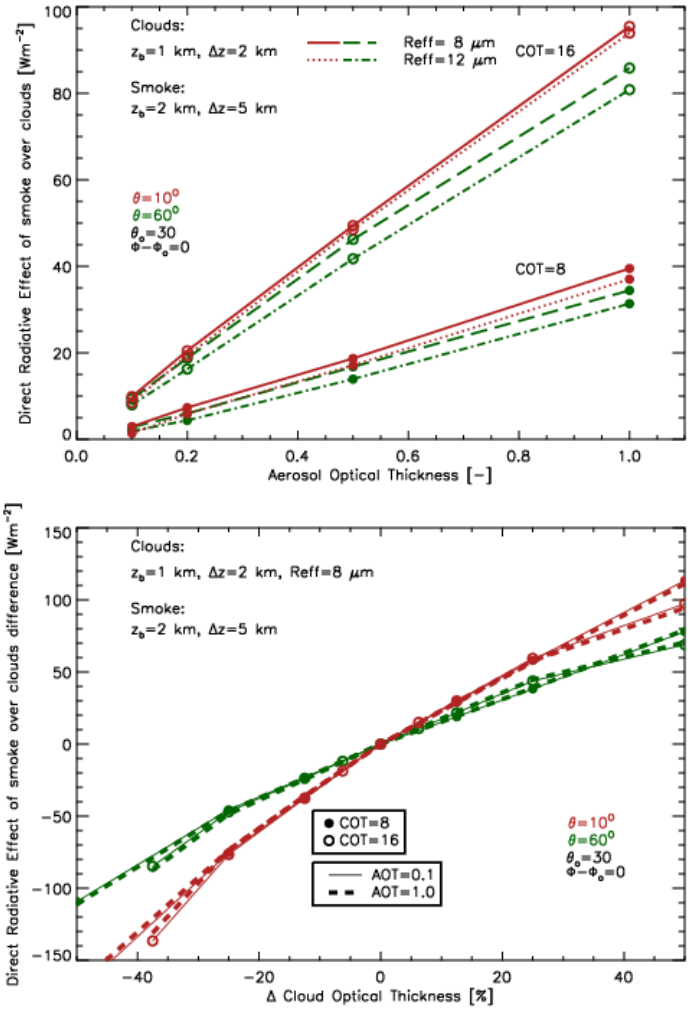

Figure 12: (a) Aerosol DRE for simulated scenes with clouds between 1-2 km and smoke aerosol between 2-5 km as a function of AOT at 550 nm. The COT was 8 or 16, the effective cloud droplet radius 8 or 12 μm. SZA was 30°, VZA was 10° or 60°, RAZI was 0°. (b) Aerosol DRE for simulated scenes as in (a), as a function of relative error in the retrieved COT.

clouds also increases, increasing the DRE. Clearly, the effect of AOT and COT on DRE are coupled. At a still relatively modest COT of 16, an increase of AOT from 0.1 to 1 increases the DRE from 10 to 95 W m^{-2}, for high AOT of 1, a doubling of COT from 8 to 16 increases the DRE from 40 to 95 W m^{-2}.

Accurate AOT and COT retrievals are clearly essential for an accurate aerosol DRE over clouds. For DAA, the effect of an error in the COT is estimated using simulated reflectances as above, shown in Figure 12b. An error of 20 % in COT can lead to an error in DRE of about 50 W m^{-2} , for COT in the range of 8–16, irrespective of the AOT. A note for DAA is in order here: The DRE is computed from the difference between a measured and simulated spectrum, which both have exactly the same COT and CER (since the simulation is done with the COT and CER retrieved from the measured spectrum). Therefore, any errors in the COT and CER retrieval have no influence on the difference between the two spectra and do not show in the DRE. However, if the COT or CER for the simulation were taken from a different measurement, however accurate, the simulated and measured spectra may be very different, giving rise to large DRE values, even without overlying aerosols. This was observed in a test where POLDER COT, regridded to the OMI grid, was used in the DRE computation, instead of the COT from the OMI-MODIS spectrum. Even though the POLDER COT was probably more accurate than the OMI-MODIS COT, the derived DRE was very erratic. For the POLDER DRE calculation this effect is different, because the DRE is computed using the scene twice with the same retrieved COT.

9.1.4 Cloud optical thickness and droplet size retrieval

The cloud microphysical parameters cloud optical thickness $\tau_{\rm cld}$ and cloud droplet effective radius $r_{\rm eff}$ can be derived from the cloud scene reflectance in the visible and the SWIR. [RD11, RD22]. In Figure 13 the effect of absorbing aerosols on this retrieval of cloud microphysical parameters is shown, following [RD12]. The top panel shows the difference between the cloud microphysical retrievals for clean (black) and smoke polluted (white) clouds using the 867 nm and 1640 nm channels, which is the wavelength pair used for many instruments like Advanced Very High Resolution Radiometer (AVHRR) [RD23], Moderate Resolution Imaging Spectroradiometer (MODIS) [RD22], Spinning Enhanced Visible and Infrared Imager (SEVIRI) [RD24] and SCIAMACHY by [RD25]. As was shown by [RD12], the TOA reflectance for a polluted cloud is lower than that for a clean cloud, due to the aerosol absorption. Therefore, without a correction for this effect, the retrieved cloud optical thickness and effective radius will be underestimated. The bottom panel shows the effect of using the 1246/1640 nm wavelength pair instead of the 867/1640 nm wavelength pair. At 1246 nm the extinction coefficient is three times lower than at 867 nm and even only 11 % of that at 555 nm. Note that an aerosol optical thickness of 0.6 at 555 nm represents a dense smoke layer. Therefore, a retrieval algorithm was set up, to retrieve cloud parameters using SWIR wavelengths only, to minimise absorbing aerosol effects from smoke.

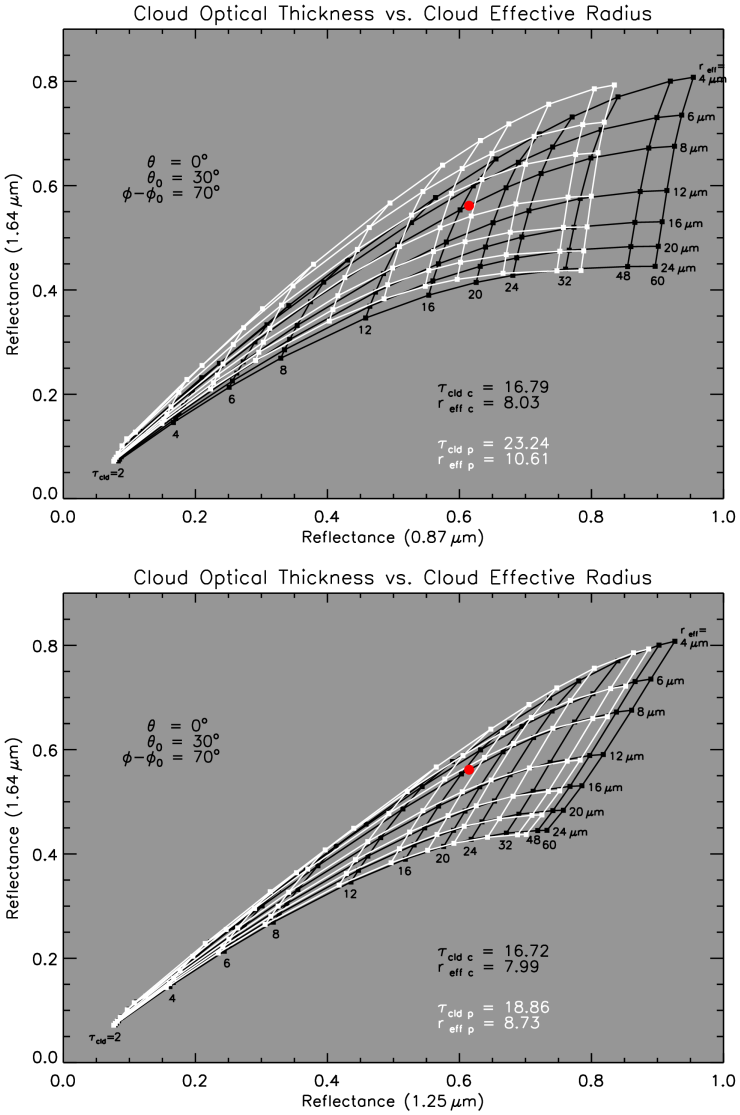

Figure 13: Clean cloud (black) and smoke polluted (white) TOA reflectances at one geometry (as given) using different channels: 867/1640 nm (top panel), and 1246/1640 nm (bottom panel).

9.1.5 Errors in cloud selection

Using a simulated polluted cloud scene, the changes in FRESCO retrievals due to aerosol absorption were assessed. The change in FRESCO CP and FRESCO CF for increasing AOT is shown in Figure 14. FRESCO CF is increasingly affected by aerosol absorption, while FRESCO CP is affected only for AOT larger than about 1.5 at 550 nm. Since the maximum AOT for smoke over the South-Atlantic Ocean is about 1.5 at 532 nm [RD26], the influence of aerosol absorption on the FRESCO CP retrieval is expected to be small. Furthermore, since cloud height has a small influence on the aerosol DRE, the error from FRESCO CP retrieval uncertainties can be neglected. The FRESCO CF is underestimated by about 0.2 for an AOT of 1.5 at 550 nm. Note that the AAI for an AOT of 1.5 at 550 nm is already as high as 9.

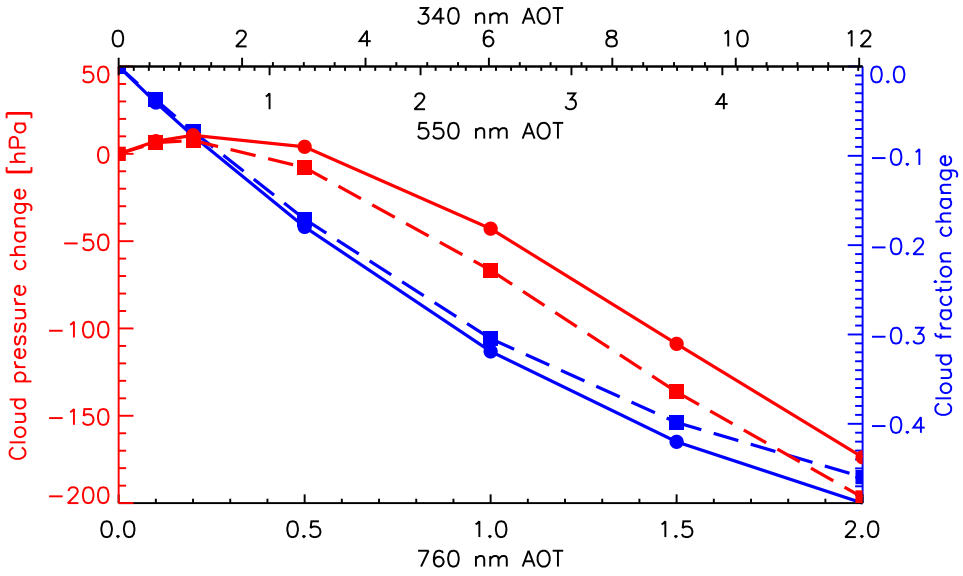

Figure 14: Change of FRESCO cloud pressure (red) and cloud fraction (blue) retrievals, for increasing aerosol load above a cloud at two solar zenith angles and nadir view. The x-axes show the AOT of the smoke layer at three different wavelengths. The water cloud, with a cloud optical thickness of 20, was placed between 1 and 2 km, while the absorbing smoke layer was placed between 4 and 5 km.

9.2 Anisotropy factor

The effect of assuming an unchanged anisotropy factor between polluted and unpolluted scenes is treated in the current section, following the analysis in [RD20]. This thesis describes the maximum uncertainty that can be expected in aerosol direct radiative effect using Eq. 7 by simulating a cloud scene with and without (smoke) aerosols above the cloud.

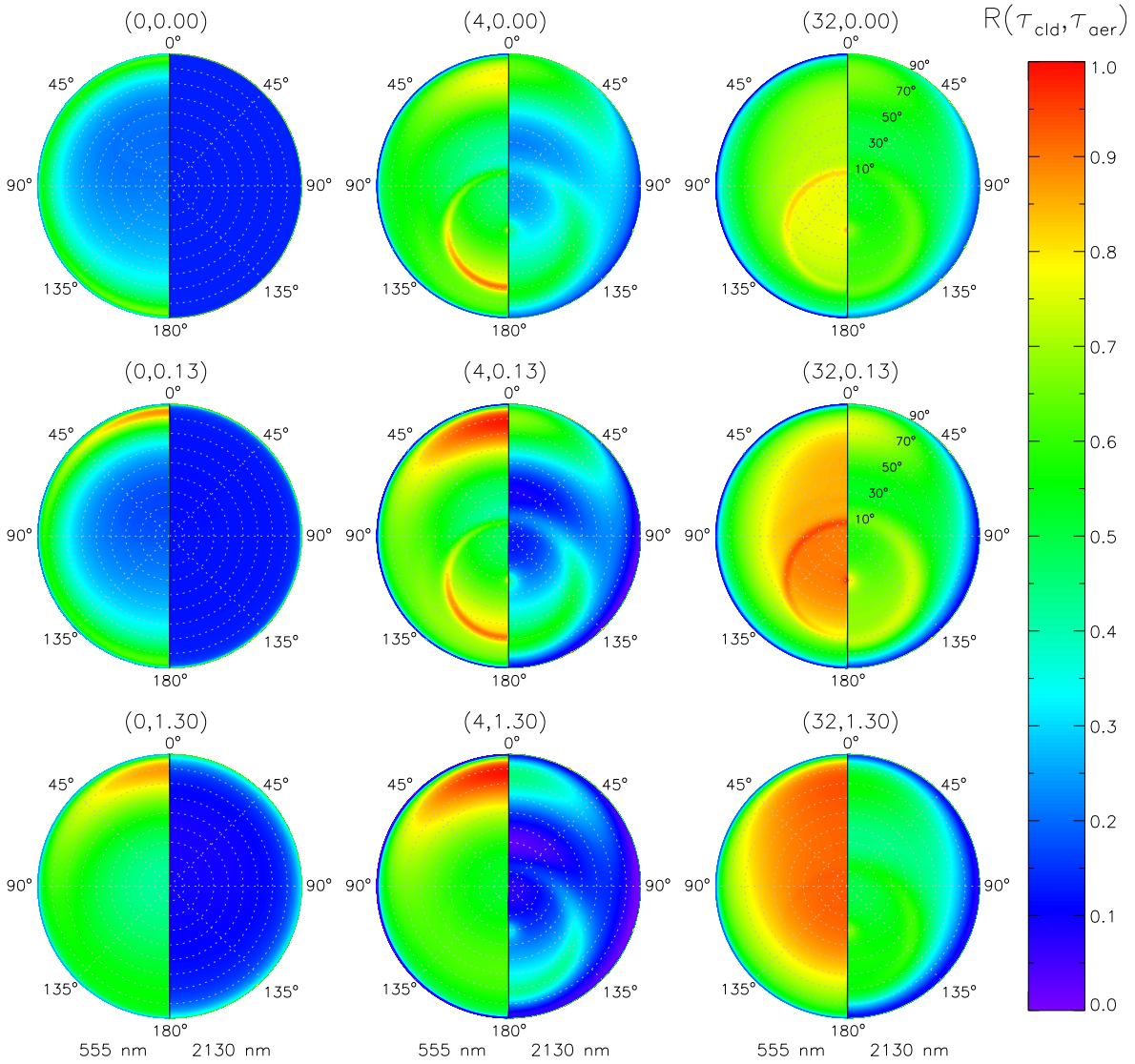

Figure 15: (left) Polar plot of the spectral BRDF of a scene as a function of viewing zenith angle (range of the polar plot) and relative azimuth angle (ϕ of the polar plot), at 555 nm (left hemisphere) and 2130 nm (right hemisphere), for different COT and AOT (given in brackets). From left to right the COT increases, while from top to bottom the AOT increases. Thus, the top-left plot represents the spectral BRDF for a Rayleigh atmosphere, while the right-bottom plot shows the spectral BRDF of an atmosphere with a cloud (COT=32) and a thick smoke layer above (AOT=1.3) at 555 and 2130 nm. (right) Spectral BRDF change ΔB^* (compared to the aerosol-free case, see Eq. 11) for the different cloud with smoke scenes, given for 555 nm. The cloud-free cases have been omitted.

The anisotropy factor B is defined as the Bi-directional Reflectance Distribution Function (BRDF) of a scene normalized by the spectral planetary albedo A, which is defined as

$$A(\lambda,\mu_0) = \frac{F^{\uparrow}(\mu_0)}{E_0(\lambda)\cdot\mu_0} = \frac{1}{\pi}\int_0^{2\pi}\int_0^1 R(\lambda;\mu,\phi;\mu_0,\phi_0)\mu\,\mathrm{d}\mu\,\mathrm{d}\phi \tag{8}$$

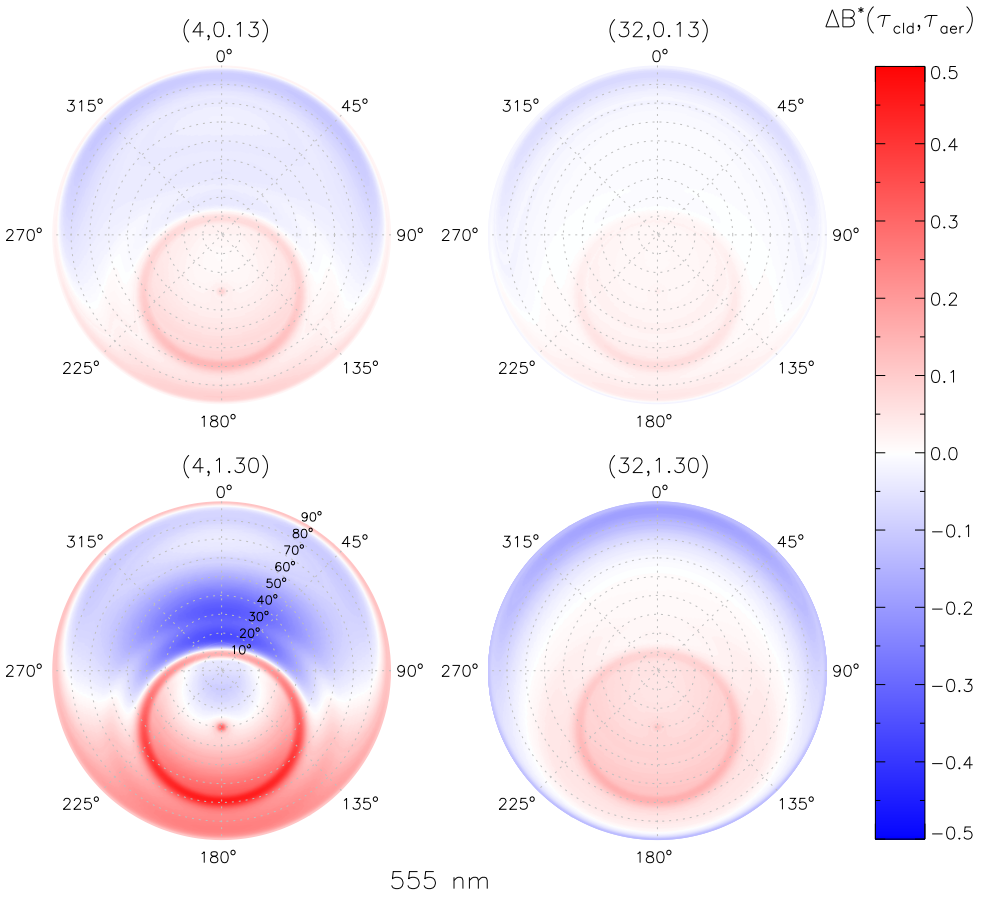

Figure 16: Spectral BRDF change ΔB^* (compared to the aerosol-free case, see Eq. 11) for the different cloud with smoke scenes in Ffig 15. The cloud-free cases and the 2130 nm parts have been omitted.

and

$$B(\lambda,\mu_0) = \frac{R(\lambda;\mu,\phi;\mu_0,\phi_0)}{A(\lambda,\mu_0)}. \tag{9}$$

The anisotropy factor of a cloud scene is strongly dependent on scattering angle, since the BRDF of a cloud scene has some strong peaks, especially in backscatter conditions (glory) and around 140° (cloud bow). It can be shown that the uncertainty in the DRE retrieval is

$$\mathrm{DRE}_{\mathrm{aer}} - \mathrm{DRE}^*_{\mathrm{aer}} = \mathrm{F}^{\uparrow}_{\mathrm{cld+aer}} \Delta B^*, \tag{10}$$

where $\mathrm{DRE}^*_{\mathrm{aer}}$ is the DRE when the actual anisotropy factor $B_{\mathrm{cld+aer}}$ is used instead of the aerosol-free anisotropy factor B_{cld}. ΔB^* is the relative difference in anisotropy factor,

$$\Delta B^*(\mu,\phi;\mu_0,\phi_0) = \frac{B_{\mathrm{cld}}(\mu,\phi;\mu_0,\phi_0) - B_{\mathrm{cld+aer}}(\mu,\phi;\mu_0,\phi_0)}{B_{\mathrm{cld}}(\mu,\phi;\mu_0,\phi_0)}. \tag{11}$$

In other words, the difference between the 'true' DRE and the DRE derived assuming an unchanging anisotropy factor B is proportional to the change in anisotropy factor $\Delta B^*(\lambda;\mu,\phi;\mu_0,\phi_0)$ only.

To estimate the uncertainty introduced by the assumption of an unchanging anisotropy factor, the BRDF for scenes with aerosols and clouds was simulated for different COT and AOT. For the simulations, a cloud was placed between 1 and 2 km and an aerosol layer between 2 and 5 km altitude. The clouds were simulated assuming a single-mode gamma particle size distribution with effective radius $r_{\mathrm{eff}} = 16\mu$m and an effective variance $v_{\mathrm{eff}} = 0.15$. For the aerosols, a bi-modal log-normal size distribution model was used, based on the 'very aged' (5 days) biomass plume found over Ascension Island during SAFARI 2000. [RD15]. A refractive index of $1.54 - 0.018i$ was used for all wavelengths longer than 550 nm. However, for the UV spectral region the imaginary refractive index was modified so that the absorption Ångström exponent was 2.91 in the UV, which fits satellite observations better [RD19]. The geometric radii for this haze plume used in the simulations

here were $r_c = 0.255$ μm and $r_f = 0.117$ μm for the coarse and fine modes, with standard deviations $\sigma_c = 1.4$ and $\sigma_f = 1.25$, respectively. The fine mode number fraction was 0.9997. These numbers are similar to the numbers used by [RD20] and the same as used in [RD4] to estimate the anisotropy change for SCIAMACHY DRE.

The results are summarized in Fig. 15 and 16. In the first figure the spectral BRDF is given for different scenes. The BRDF is symmetric about the 0–180° axis, but here the left side of each polar plot shows the BRDF at 555 nm, and the right side the BRDF at 2130 nm. The nine plots show the spectral BRDF for scenes with different AOT and COT, indicated by the (AOT, COT) number pairs above the figures. The COT increases from left to right from 0 to 4 and 32, while the AOT changes from top to bottom between 0, to 0.13 and 1.3. In the left-top plot the BRDF for a Rayleigh atmosphere is shown, the right-bottom plot show the BRDF for a thick cloud with a thick smoke plume.

The difference between the left side and right sides of the polar plots show that the largest geometrical dependence of the BRDF are found at smaller wavelengths. The BRDF is more pronounced for 555 nm compared to 2130 nm. Consequently, the effect of overlying smoke aerosols on ΔB^* is small for longer wavelengths. However, at 555 nm the effect is significant. The BRDF of cloud scenes is strongly depending on the scattering angle, with a large concentration of radiation especially in the backscatter direction and at 140° degrees. When the AOT of an overlying aerosol layer increases, these strong peaks are smoothed out, and the change in $\Delta B*$ is significant. The effect is largest for a thin cloud and thick aerosol layer (COT=4, AOT=1.3).

In Fig. 16, the change in cloud BRDF due to overlying smoke aerosols ΔB^* at 555 nm is given, for all the scenes in the left panel with aerosols and clouds (the scenes with COT=0 have been omitted). The same figures can be given at 2130 nm, but since the changes are much smaller, they are also omitted. The right panel shows again the largest change in ΔB^*, and thus DRE, for a thin cloud and thick aerosol layer, for geometries in the cloud bow.

The maximum DRE change was found for this situation (COT=4, AOT=1.3, single scattering angle=140°). The DRE changed from -8.0 to 3.7 Wm^{-2}. This is a moderate change, smaller than the uncertainty estimated above, but due to the low COT the DRE is small, and the DRE changes sign because of the assumption of an unchanging anisotropy factor. This underlines the fact that the DAA method is valid only for sufficiently clouded scenes. Therefore, a minimum cloud fraction of 0.3 is always applied to the scenes to derive the DRE.

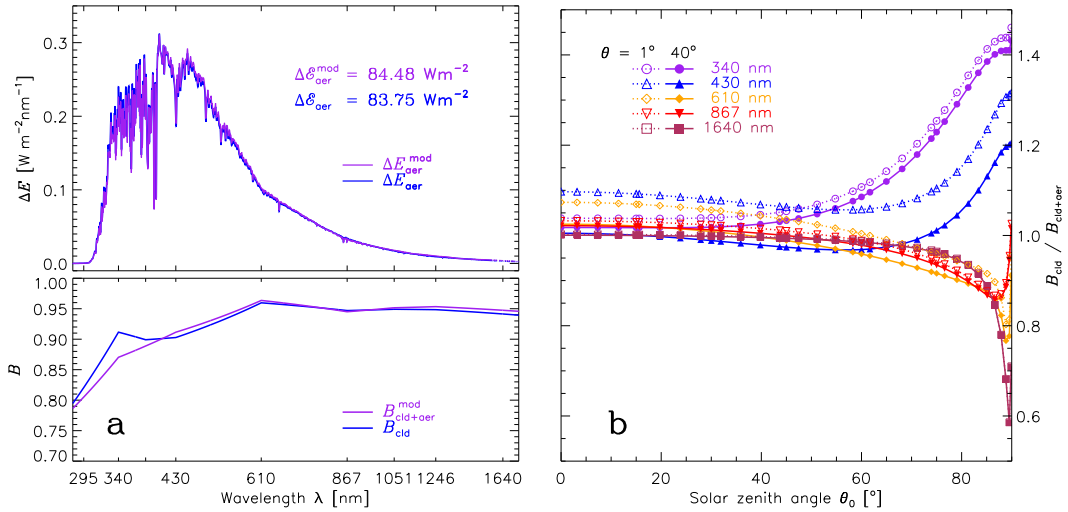

Figure 17: Changes in the anisotropy factor due to aerosols in the scene. a) Top panel: Net irradiance change (absorbed energy) as a function of wavelength for a scene on 10 August 2006 at 09:13:51.89 UTC. The blue curve shows the irradiance change using the anisotropy factor of the modelled aerosol-unpolluted cloud scene $B_{\rm cld}$ as in equation (7), while the purple curve shows the irradiance change with the actual (modelled) aerosol-polluted cloud scene anisotropy. Bottom panel: Anisotropy factor for the modelled unpolluted cloud scene $B_{\rm cld}$ (blue) and the modelled polluted cloud scene $B_{\rm cld+aer}$ (purple). b) Anisotropy change as a function of solar zenith angle for selected wavelengths due to the presence of the aerosols. The modelled scene was the same as in a). The dotted lines with open symbols show the anisotropy change for a viewing zenith angle of 1°. The solid line with filled symbols shows the anisotropy change for a viewing zenith angle of 40°.

Consequently, the derived DRE is always positive. Also note that the scattering angle of 140° is a common angle in the measurements, occurring about 40 % of the time for measurements over the southeast Atlantic during summer, so low DRE values could easily be affected by this uncertainty. Furthermore, cloud parameter retrievals can be biased in these conditions [RD21], but the effects are small at SWIR wavelengths (see Fig. 15) and are neglected for the cloud retrieval. ΔB^* is small for all other situations.

From the model results the anisotropy factor of the aerosol-polluted cloud scene $B_{\mathrm{cld+aer}}$ can now be determined for any geometry. For the scene shown in Figure 11 the anisotropy factor of the aerosol-polluted scene is slightly different from that of the aerosol-unpolluted cloud scene, see Figure 17a. As mentioned above, the optical thickness of the aerosol layer τ_{aer} was fitted so that the aerosol DRE, using equation (7), was the same for the modelled aerosol-polluted cloud scene as for the measured scene (84 Wm^{-2}). When the actual anisotropy factor of the modelled aerosol-polluted cloud scene was used, as in equation (6), the aerosol absorption shifts slightly from the UV to more visible wavelengths (see top panel in Figure 17a). Since the peak of the solar irradiance is in the visible, the total aerosol DRE increased by 0.9% (from 83.75 to 84.48 Wm^{-2}).

A modelling study showed that the angular redistribution of scattered radiation by aerosols is dependent on τ_{aer}, wavelength and geometry. The dependence on τ_{aer} is linear, with an increasing change for increasing τ_{aer}. The change in anisotropy as a function of solar zenith angle is given in Figure 17b for several wavelengths. It is relatively small at any wavelength and viewing zenith angle for solar zenith angles below 60°. For larger solar zenith angles the change can be larger.

10 Validation

Validation of the instanteneous aerosol DRE has been performed in several ways. The DRE is available from SCIAMACHY and OMI-MODIS reflectances, as described in this ATBD and direct comparisons have been made between the retrievals from SCIAMACHY and OMI-MODIS. The similarity and differences between the data sets from both (sets of) instrument were investigated in [RD7]. Figure 18 shows the high correlation between the two retrievals from comparison of the DRE in the outflow region of smoke from Africa over the southeast Atlantic.

In particular, the averaged instantaneous aerosol DRE over clouds was found to be very high during the biomass burning season, much higher than found from general circulation models (GCMs) [RD27]. Even though the satellite measurements over clouds represent the instantaneous direct effect, and not the daily averaged aerosol forcing normal for GCMs, the instantaneous effects were also strongly underestimated by the models. The comparison with moxdel results and the lack of reproducing the observations in a GCM is described in section 10.1. Next, the OMI-MODIS DRE was compared to instanteneous aerosol DRE from POLDER measurements [RD28], which were determined using the AOT over clouds that are possible by the different polarisation effects of aerosols and clouds [RD29]. This is an altogether different way of retrieving the aerosol DRE over clouds, derived from simultaneous above-cloud AOT and cloud parameter retrievals, making a computation of the aerosol DRE possible over clouds. A comparison with SCIAMACHY and OMI-MODIS derived DRE showed even higher DRE values from POLDER measurements. Lastly, a comparison with above-cloud AOT from SEVIRI measurements is shown to be highly correlated with OMI-MODIS DRE in section 10.2.

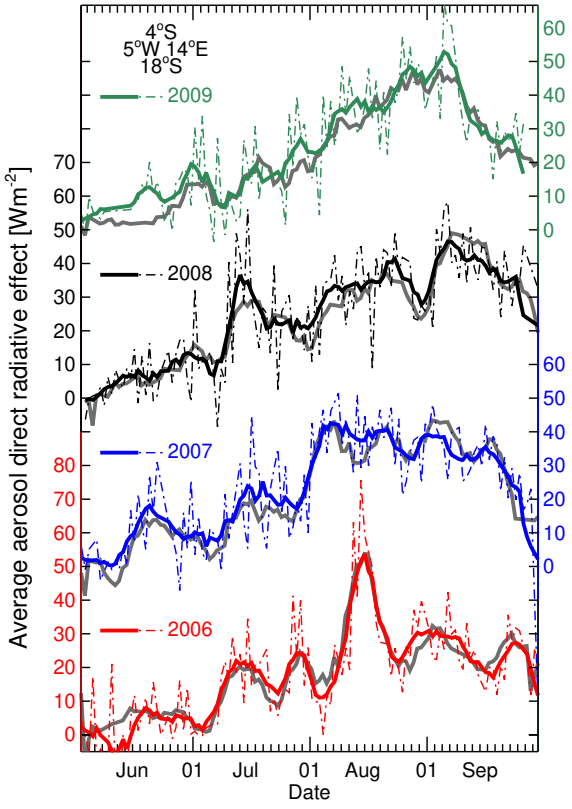

Figure 18: Area-averaged instantaneous aerosol DRE in Wm^{-2} for the region 4 to 18° S; 5° W to 14° E (local overpass times from about 12:30–14:00 UTC) in 2006–2009 (thin lines) and its 7-day running mean (bold lines) in colored lines for all OMI-MODIS pixels with CF>0.3 and CP>800 hPa. In bold grey the SCIAMACHY (local overpass times from about 09:00–10:30 UTC)area averaged 7-day running mean aerosol DRE is plotted for CF>0.3, CP<800 hPa.

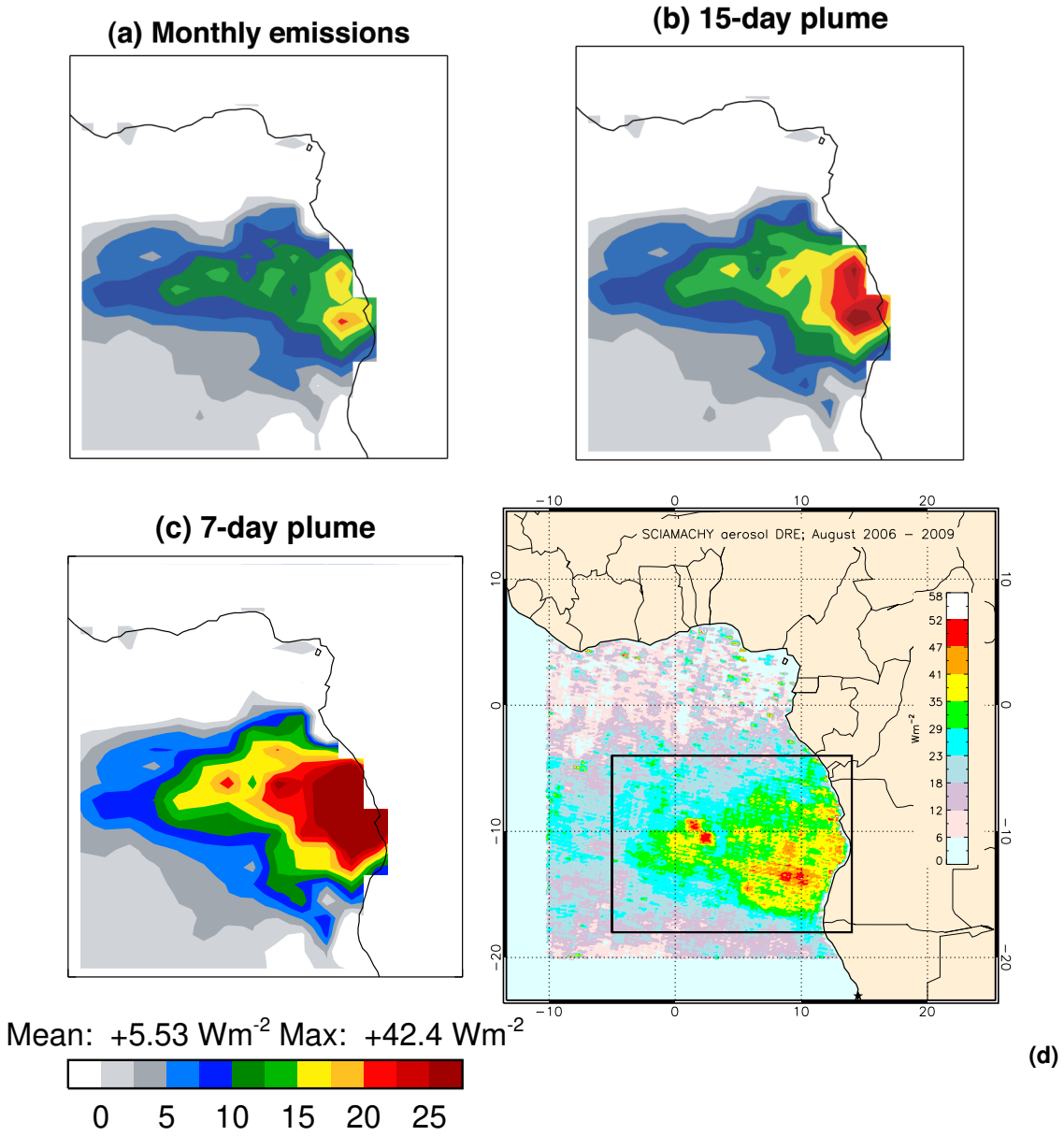

Figure 19: (a) HadGEM2 modeled cloud-sky shortwave aerosol direct radiative effect in Wm^{-2}, averaged over 1–8 August 2006 at 9:30 local time for cloud cover larger than 0.3. The mean aerosol DRE over clouds for this experiment averaged over the whole month is 3.80 Wm^{-2}. (b) Same as (a) but with emissions distributed over a 15-day period. Monthly mean is 5.94 Wm^{-2}. (c) Same as (a) but with emissions distributed over a 7-day period. Monthly mean is 5.64 Wm^{-2}. d) Average SCIAMACHY aerosol DRE over marine water clouds for August 2006 – 2009. The rectangle indicates the main outflow region during the biomass burning season.

10.1 Comparison to model results

The DRE values found in Fig. 18 are higher than found for this region in September 2000 in a comparative study between GCMS, using SAFARI-2000 data to constrain radiative model computations. A maximum of 65 Wm^{-2} was found in the models [RD30]). SCIAMACHY DRE values were compared to model calculations from the HadGEM2 model [RD27], to investigate the discrepancies between models and observations.

The main outflow region is the area between about 4° to 18°S and 5°W to 14°E, depicted by the rectangle in Figure 19d. This is well captured in the models. However, the emission of smoke from Africa was strongly peaked in August, while in the model a continuous monthly averaged emission was assumed. This creates discrepancies, but not enough to eplain the differences with the observations. In Figure 19b and c the effects are illustrated when emission are modelled as short, intense aerosol 15-day or 7-day averaged plumes. The increased the maxima twofold with a fourfold increase of emission rate. However, accounting for such episodic emissions in models did not explain the difference in aerosol effects in models and observations by SCIAMACHY and OMI-MODIS.

Instead, the discrepancy was caused by an underestimation of the absorption in the UV and the brightness of the clouds, which both have to modelled well. A theoretical study by [RD31] showed the extreme range of aerosol effects that can be expected in scenes with and without clouds and smoke. In Fig. 20 simulations are presented of the instantaneous aerosol DRE at the Top-Of-Atmosphere (TOA) for different scenes in which clouds or aerosols (smoke) is present at different levels. All computations were performed over a dark surface (like an ocean) using a solar zenith angle of 30°. For such scenes introducing an (absorbing) aerosol layer has a cooling effect, since scattering dominates over absorption even for dark aerosols like smoke and the aerosol layer increases the amount of light reflected from the scene. However, clouds can completely change this picture, which is illustrated in the next scenes in Fig. 20. The highest aerosol direct effects are found when clouds underly the aerosol layer, because the clouds increase the amount of scattered light, which is then absorbed in the aerosol layer. This is what is happening in the observations by SCIAMACHY and OMI-MODIS

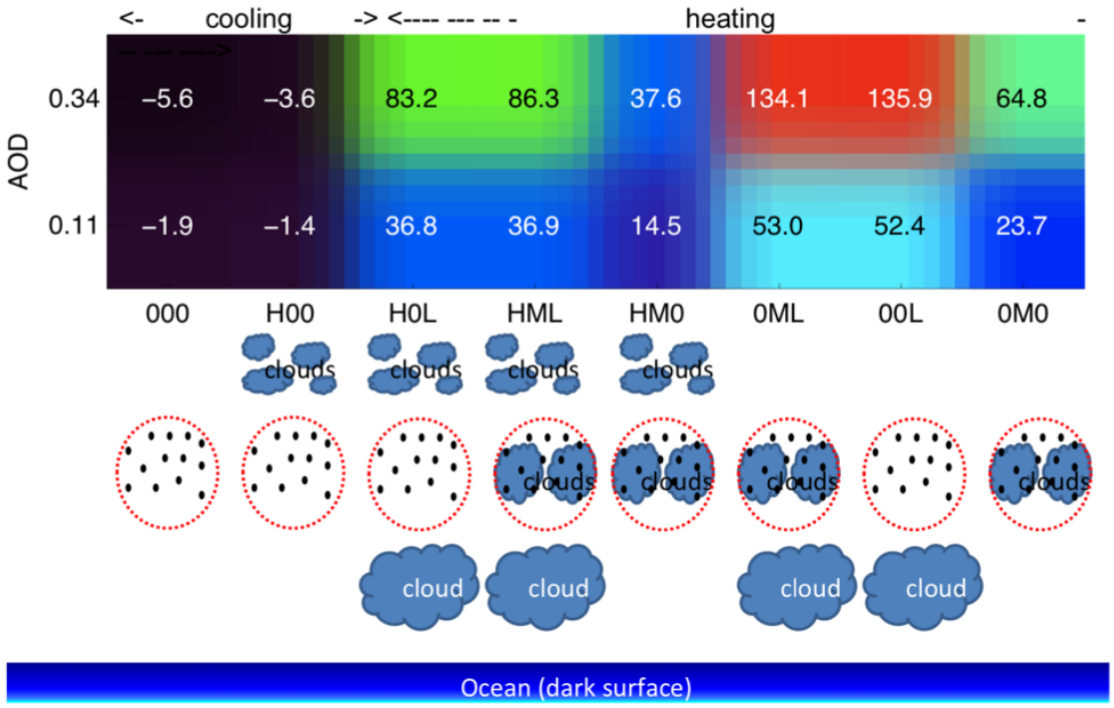

Figure 20: Theoretical cases of vertical structures of aerosols and clouds. For each case the TOA shortwave aerosol radiative forcing is simulated with the radiative transfer code Matrix Operator MOdel (MOMO), for a small (AOT=0.11) and large (AOT=0.34) amount of aerosols, in a clear scene and for scenes with overlying clouds and/or mixed clouds and/or underlying clouds over a dark ocean surface. The displayed values are instant shortwave TOA direct effects for SZA=30°, the aerosol macroscopic properties are those of biomass burning aerosols.

DRE, when cloud scenes are selected, in which an amount of smoke is present that can create such high DRE values. High clouds, like cirrus, generally reduce the aerosol effects from underneath.

10.2 Comparison with DRE and above-cloud AOT from satellites

Finally, the DRE retrievals from OMI-MODIS and SCIAMACHY could be verified with retrievals from different satellite instruments, which were able to retrieve above-cloud aerosols. The comparison with POLDER and SEVIRI measurements are discussed next.

10.2.1 Comparison with POLDER DRE

POLDER is a passive optical imaging radiometer and polarimeter on-board the Polarization and Anisotropy of Reflectances for Atmospheric Science coupled with Observations from a Lidar (PARASOL) [RD32]. Using POLDER measurements, the above-cloud AOT, the aerosol Single Scattering Albedo (SSA) and the COT were retrieved in two steps. The first one consists of using the polarization radiance measurements to retrieve the scattering AOT and the aerosol size distribution in a cloudy scene. Aerosols affect the polarization in a cloudy scene in two ways. Firstly, the large peak of the signal around a scattering angle of 140°, caused by the liquid cloud droplets, is attenuated. Secondly, an additional signal at side scattering angles is created. The spectral contrast and the magnitude of the total radiances measured in the visible and SWIR are used to retrieve the absorption AOT and COT simultaneously [RD33]. The POLDER DRE was finally calculated over the southeast Atlantic for aerosols over clouds in 2006 using the retrieved AOT, SSA and COT with the method described in section 3 of [RD29].

The POLDER DRE was compared to the DRE sets from OMI-MODIS and SCIAMACHY in [RD28]. SCIAMACHY was fully operational on ENVISAT in 2006, while OMI was flying on Aura and MODIS on Aqua as part of the Afternoon satellite constellation A-Train. Details from all four instruments are given in Table 2.

In Figure 21a, the area-averaged instantaneous aerosol DRE over clouds from the three data sets is given for all available data in the area 10°N to 20°S,10°W to 20°E, between 1 June and 1 October 2006. This is the biomass burning season and the events during this period have been investigated often before [RD34, RD19, RD35]. In the selected region high area-averaged DRE values have been reported during this season [RD26, RD27, RD36, RD29]. Since the instruments have different overpass times, the instantaneous aerosol DRE over clouds was normalized by dividing by the cosine of the solar zenith angle. Therefore, the quantity in Figure 21a represents the instantaneous aerosol DRE for an overhead Sun (at noon), which is generally higher than the instantaneous aerosol DRE measured during the overpass. Figure 21a shows the evolution of the biomass burning season in 2006, with low DRE values in June, high values in July, extreme values in August and moderate values in September. The area-averaged DRE of smoke over clouds reaches values up to 100 W m^{-2} and more in mid-August 2006, according to SCIAMACHY and POLDER. On the other hand, the average OMI-MODIS DRE is never higher than about 60 W m^{-2}.

In Figure 21b the noon-normalized area-averaged instantaneous DRE over clouds over the southeast Atlantic is shown, like in Figure 21a, but using only those pixels that are covered by all three instruments. This effectively removes all sampling issues and differences due to different cloud screening strategies for the instruments. Note that at a number of days no values were available, since there were no areas with DRE that are sampled by all three instruments. This underlines the importance of sampling, even for such a fairly large area. The number of pixels over which was averaged per day is shown in the lower panel of Figure 21b. The correlation between the noon-normalized area-averaged instantaneous DRE from the three instruments is now significantly improved compared to Figure 21a. The aerosol DRE from OMI-MODIS follows the aerosol DRE

Table 2: Spatial and temporal resolution of the different satellite instruments as used in this paper. Grid sizes of SCIAMACHY and OMI are those at nadir, grid sizes of POLDER and MODIS are fixed.

Instrument	Platform	Local equator crossing time	Global coverage (days)	Pixel size (km × km)	Operation period
POLDER	PARASOL	13:33	1	6×6	2004 – 2013
SCIAMACHY	EnviSat	10:00	6	60×30	2002 – 2012
OMI	Aura	13:38	1	13×24	2004 – present
MODIS	Aqua	13:30	1	0.5×0.5	2002 – present

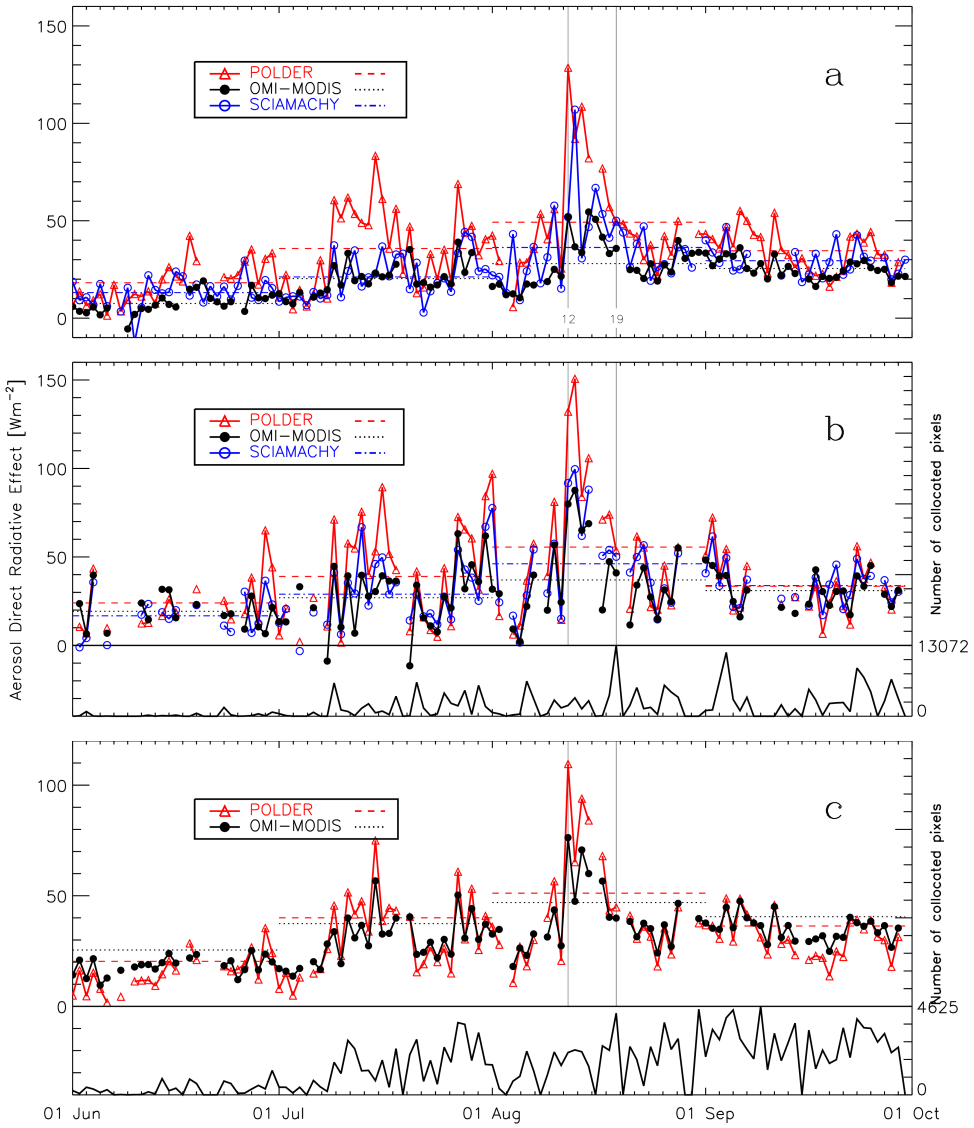

Figure 21: (a) Noon-normalized instantaneous aerosol DRE over clouds from combined OMI-MODIS reflectances (black), SCIAMACHY reflectances (blue) and POLDER AOT and COT retrievals (red) from 1 June - 1 October 2006, averaged over the area 10°N to 20°S;10°W to 20°E in the southeast Atlantic. The average monthly aerosol DRE over clouds are given by the coloured straight lines during each month. (b) Same as (a), but for OMI-MODIS and SCIAMACHY pixels that were regridded to the 6×6 km^2 POLDER grid. Averaged values were only calculated from grid points that were covered by all three instruments. The number of collocated pixels that are covered by all three instruments is given in the lower panel in (b). (c) Area-averaged instantaneous aerosol DRE from OMI-MODIS and POLDER regridded to the OMI footprint. Note that because SCIAMACHY is omitted the number of pixels is much larger than in (a) and (b), and furthermore, the DRE is not noon-normalized, because the overpass time of OMI, POLDER and MODIS are similar.

from SCIAMACHY very closely for almost the entire period shown, in line with the results in Fig. 18. Note that the maximum DRE from OMI-MODIS is now increased to almost 90 Wm^{-2}, which was due to removing many pixels with a moderate to low DRE during mid-August, that were not covered by POLDER and SCIAMACHY.

Additionally, the sampling was checked by gridding the finer POLDER data to the coarser OMI grid and sampling only pixels that were covered by both OMI-MODIS and POLDER. In this case SCIAMACHY was omitted, so as not to lose too many POLDER and OMI-MODIS pixels because of the coarse SCIAMACHY grid. The smaller POLDER pixels were averaged over the OMI footprint using a 2D Gaussian weighting function. This procedure is exactly the same for the averaging of MODIS pixels in an OMI footprint in the OMI-MODIS DRE computation, and described in detail in [RD9]. Figure 21c shows the area-averaged instantaneous aerosol DRE over clouds from collocated OMI-MODIS and POLDER pixels sampled on the OMI grid. Obviously, gridding to the OMI grid instead of to the POLDER grid does not change the results very much, but without SCIAMACHY the large number of pixels that are collocated results in a very high consistency between OMI-MODIS and POLDER DRE. Furthermore, without SCIAMACHY the noon-normalization is no longer necessary because the overpass times of OMI, MODIS and POLDER are very close, and Figure 21c shows the instantaneous local DRE during overpass. The figures show that POLDER DRE is higher than OMI-MODIS DRE, especially for high values, but also lower for low values.

This is also clear from a scatterplot of collocated POLDER DRE vs. OMI-MODIS DRE for regridded POLDER pixels, shown in Figure 22. The figure shows a good correlation between collocated POLDER and OMI-MODIS DRE, but with higher values for POLDER, especially for DRE larger than 100 Wm^{-2}. An average ratio of OMI-MODIS DRE to POLDER DRE of 0.82 was found, while a normal linear least-squares fit (shown by the red line in Figure 22) yields a slope of OMI-MODIS to POLDER ratio of only 0.7. This is because the fit is dominated by the large values, while the large majority of points are moderate values around 25 W m^{-2}. When a fit is drawn which is weighted to the deviation from this moderate value (shown by the green line), a slope of 0.99 is found, showing that the aerosol DRE over clouds is the same from POLDER and OMI-MODIS for moderate values.

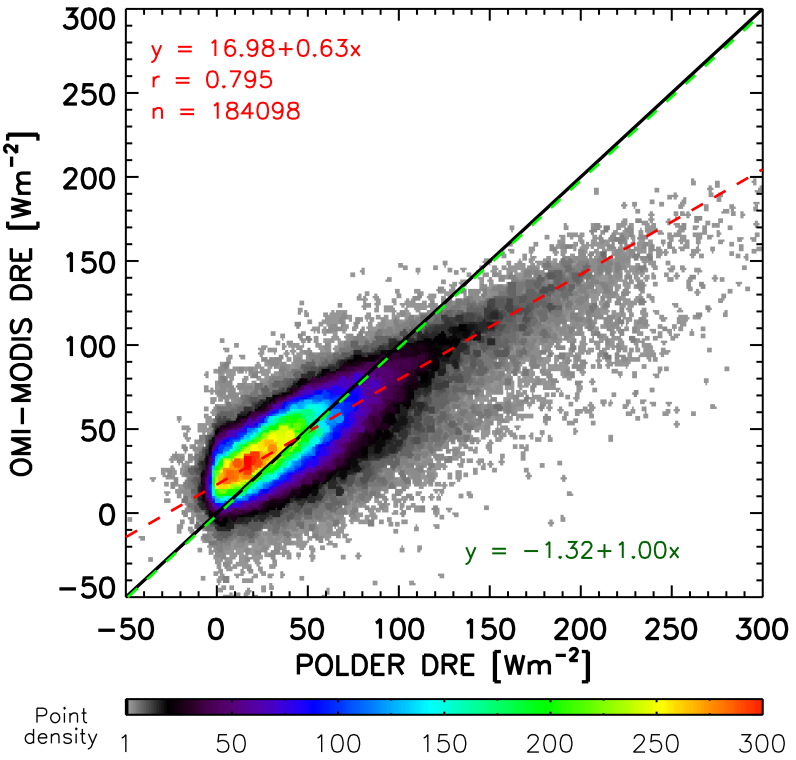

Figure 22: Scatterplot of POLDER DRE versus DRE from regridded OMI-MODIS data. The red dashed line shows an unweighted linear least-squares fit, the green dashed line shows a linear least-squares fit weighted by the distance to the average value of 25 Wm^{-2}.

10.3 DRE compared to AOT during the 2016 and 2017 biomass burning season

The instantaneous DRE in a cloudy scene can also be directly related to the above-cloud aerosols (ACA) AOT, using a simple approximate expression, given by [RD37] for the change in albedo at TOA $\Delta\rho$ due to an aerosol layer versus the albedo of the surface underneath:

$$\Delta\rho = \rho - \rho_s = \tau(\omega_0(1-g)(1-g)^2 - 4(1-\omega_0)\rho_s) \tag{12}$$

where ρ is the albedo at TOA, ρ_s the surface albedo, τ the aerosol optical thickness, ω_0 the single scattering albedo and g the aerosol aymmetry factor. Approximate values can be established for the aerosol parameters and surface albedo, but in general Eq. 12 indicates a direct relationship between the aerosol optical thickness and the DRE. If the surface albedo is assumed to be the (constant) cloud brightness and taking into account that cloud height has a very small impact on the reflectance at TOA [RD38], and neglecting the part of the AOT in clear scenes and the scattering part, the ACA AOT and instantaneous DRE in cloudy scenes should be reasonably linearly correlated.

This is illustrated in Fig. 23. The OMI-MODIS DRE in panel (a) is compared to Above-Cloud Aerosols (ACA) retrievals derived from MODIS [RD13] (solid line) and OMI [RD42] (dashed line) measurements in panel (b), for the biomass burniung seasons in 2016 and 2017. The correlation between the above cloud AOT and aerosol DRE over clouds is very large, especially for the MODIS ACA. Although the aerosol DRE is mainly determined by the cloud reflectance of the cloud underneath the clouds, the correlation can be explained by the persistence of the marine boundary layer clouds over the Atlantic. These clouds are very stable, and the change in cloud fraction is small when averaged over the considered areaThe large peaks in August 2016 are visible in the ACA and DRE data, and are caused by the presence of smoke.

The high values of the aerosol DRE and ACA in August and September 2016 are also reflected in AOT data collected by the AERosol RObotic NETwork (AERONET) station on Ascension Island, located at 8° S, 14.4° W. The version 2 (V2) level 1.5 AOT at 500 nm over Ascension Island from 1 June to 1 October 2016 and 2017 is shown in Fig. 23b. It shows AOT higher than 0.2 in a few isolated events in August 2016, which were strongly correlated with episodes of high aerosol DRE over clouds in the southeast Atlantic, as shown in Fig. 23a. In 2017, on the other hand, the aerosol DRE values were more moderate, and do not correlate clearly with the AOT over Ascension Island. Note that version 3 (V3) data are also available [RD43], but the level 1.5 AOT data showed rather different behaviour to the V2 data, and the V2 data were retained. Level 2.0 data were also available for 2016, but these are almost equal to the level 1.5 data, and for 2017 the level 2.0 data were not yet available. Therefore, V2 level 1.5 data were used in Fig. 23.

The peaks in AOT over Ascension Island lag the peaks in DRE and ACA over the Atlantic by two days. This is shown for 7 August 2016 (vertical line in Fig. 23). The events of these days are also illustrated in Fig. 1, which presents backtrajectories of the high DRE events during three days: 5, 6, and 7 August 2016. Clearly, the high values are corresponding to smoke from fires in Africa, which is lifted to the free troposphere at around 2000 m altitude, above the clouds, travelling westward over the Atlantic. On 5 August the aerosol DRE and AOT over the Atlantic Ocean peak (Fig. 23a and b), while the AOT over Ascension peaks on 7 August (Fig. 23c).

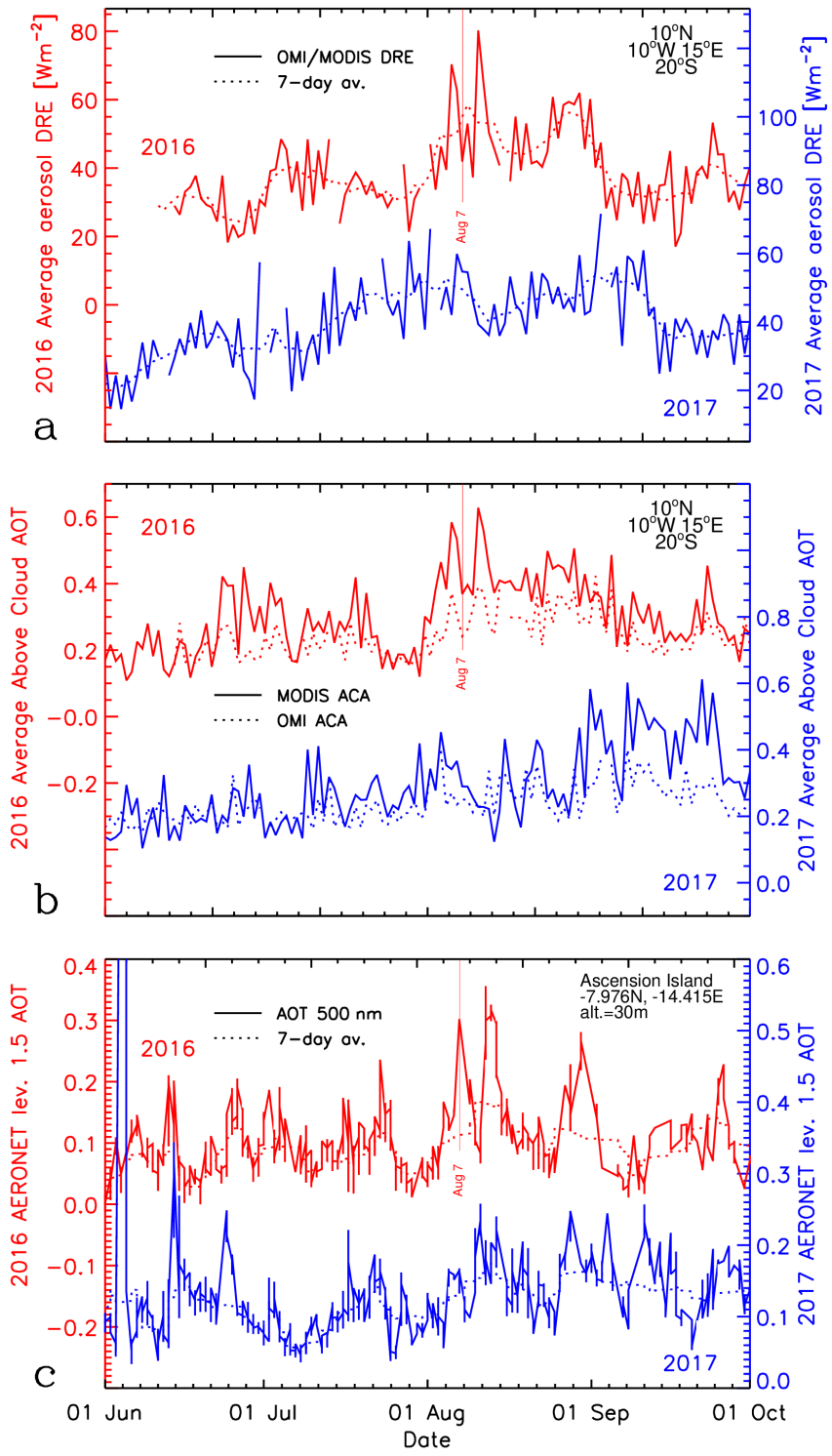

Figure 23: (a) OMI-MODIS aerosol DRE over clouds, averaged over the Atlantic Ocean (10° N to 20° S; 10° W to 15° E) in 2016 (red) and 2017 (blue). The solid line shows the area-average instantaneous DRE, the dashed line shows a 7-day running mean; (b) Above-cloud AOT (ACA) derived from MODIS (solid line) and OMI (dashed line) measurements during 2016 (red) and 2017 (blue), averaged over the same area as (a); (c): AERONET AOT at 500 nm from Ascension Island station at 7.98° S, 14.42° W in 2016 (red) and 2017 (blue). The solid line shows all available level 1.5 data, the dashed line shows a 100 point running mean.

10.3.1 Comparison with SEVIRI Above-Cloud Aerosol Optical Thickness

Lastly, ACA AOT derived from SEVIRI, on the geostationary satellite MSG, is compared to OMI-MODIS DRE in 2017 over the southeast Atlantic Ocean. SEVIRI ACA AOT were derived following [RD39] describing a simultaneous retrieval of AOT, COT and CER using the channels 0.64 μm, 0.82 μm and 1.6 μm, instead of the operational CLAAS-3 SEVIRI cloud data. Figure 24 shows a strong correlation of the ACA AOT and instantaneous DRE due to aerosols in the four months of 2017, with an arbitrary scaling between the two. In these data from 2017 a similar seasonal cycle as before can again be observed, again illustrating the strong influence of the biomass burning smoke on the clouds and the TOA radiation in this region.

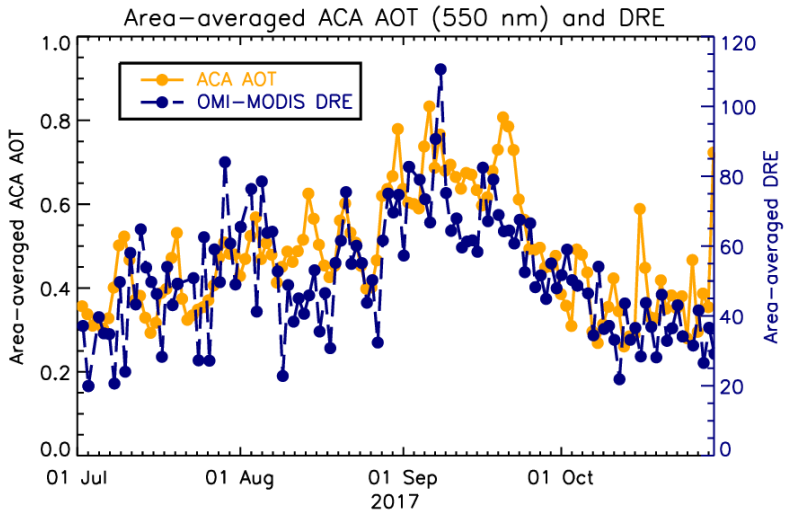

Figure 24: Above-Cloud Aerosols AOT at 550 nm (orange) and OMI-MODIS instantaneous Direct Radiative Effect (DRE, dark blue), averaged over 10 to 20°S and 5 to 15°E, from July to October 2017. The ACA AOT data were averaged each day at 13:00.

11 Conclusion

The instanteneous aerosol direct radiative effect (DRE) over clouds can be retrieved from collocated OMI and MODIS reflectance spectra of cloudy scenes, described in this ATBD. The aerosol DRE can be very high in the case wheer bright water clouds underlie dark absrbing aerosols. The random error of the OMI DRE is 12 Wm^{-2}, while comparison with POLDER shows that the OMI DRE may be underestimated for high values. The OMI DRE is available online from the TEMIS website *www.temis.nl*.